Supporting Information: Holocene-like summer climate during Marine Isotope Stage 11 in northwestern Greenland

John Michael N. Aguilar[1,2], Elizabeth K. Thomas[1]*, Diana S. Aga[2], Paul R. Bierman[3,4], Jason P. Briner[1], Isla S. Castañeda[5], Andrew J. Christ[3,a]

[1]Department of Earth Sciences, University at Buffalo, The State University of New York, Buffalo, NY, 14260, USA

[2]Department of Chemistry, University at Buffalo, The State of University of New York, Buffalo, NY, 14260, USA

[3]Rubenstein School of the Environment and Natural Resources, University of Vermont, Burlington, VT 05401, USA

[4]Gund Institute for Environment, University of Vermont, Burlington, VT 05401, USA

[5]Department of Earth, Geographic and Climate Sciences, University of Massachusetts, Amherst, MA 01002, USA

[a]currently at: U.S. Reinsurance Analytics, Aon plc, Denver, CO 80206, USA

*Corresponding author: Elizabeth Thomas (ekthomas@buffalo.edu)

Contents of this file

Introduction

This document includes detailed descriptions of methods and settings, as well as supporting figures, tables, and schematic diagrams of the methods.

Text S1. Setting

Camp Century (77.1667°N, -61.1333°E), established by the U.S. Army in northwestern Greenland (Figure 1A) during the Cold War (1960–1966 CE), served as a secret base. In 1966, the first ice core drilled to the bed of an ice sheet was collected as part of the camp's projects. The core included 1368 m of glacial ice, 14 m of debris-laden basal ice, and 3.44 m of sub-glacial sediments (Bierman et al., 2024; Christ et al., 2021). The ice–sediment interface was 530 ± 30 m above sea level (Morlighem et al., 2017). This ice core provided a 100,000-year paleoclimate time series (Dansgaard et al., 1969), though the basal sediments remained largely unstudied and were stored for decades until they were sampled for this project (Text S2.1).

The closest weather station to Camp Century site is at Pituffik Space Base (formerly Thule Air Base, 76.5311°N, -68.7033°E, 77 m above sea level, 215 km west-southwest of Camp Century). Pituffik mean summer (June to Aug) air temperature from 1950–2000 CE was 1.3 ± 0.2°C and mean annual air temperature was -14.2 ± 0.5°C (Hersbach et al., 2020). Monthly precipitation isotope observations are available for 1966–1969 CE (IAEA/WMO, 2015). For that period, the months above freezing (June to August; JJA) receive more precipitation (40.1 ± 2.3 m precipitation per month) than the rest of the year (21.9 ± 0.9 cm precipitation per month) and have relatively ^{2}H-enriched values of -142 ± 5 ‰ for JJA compared to mean December to February values of -231 ± 11 ‰ (IAEA/WMO, 2015).

Text S2. Methods and Approach

S2.1 Sediment core collection

The ice-basal sediments from the Camp Century ice core were collected in 1966 CE, cut into ~10-cm-thick subsamples, and stored frozen (-30°C) initially at the University at Buffalo (1966–1993 CE) and then at the Niels Bohr Institute (1993–2019 CE). The sediment core is divided into five units based on sedimentology (Bierman et al., 2024; Christ et al., 2023; Collins et al., 2024). The core-cutting method we employed in 2021 was designed to ensure the integrity and orientation of samples, minimize contamination, and maintain light exposure conditions suitable for various analyses. Details are in Bierman et al. (2024) and are described here briefly. Frozen core segments were cut into oriented sub-samples using diamond band and wire saws, with ethylene glycol as a cutting fluid for some samples and special care taken to avoid glycol contamination when necessary. Each sub-sample was processed under red light to preserve its luminescence properties and stored at -30°C until transfer. The samples were then transported under strict frozen conditions to multiple laboratories for detailed analyses, including luminescence measurements, paleomagnetic studies, lipid biomarker and geochemical assessments, ensuring the highest fidelity in data collection and preservation.

As detailed in Bierman et al. (2024), samples for lipid biomarker analyses were the fine (<64 μm) fraction retained after sieving for macrofossils, cosmogenic ^{10}BE, ^{26}Al, ^{21}Ne quartz ^{36}Cl feldspar, meteoric ^{10}Be, diatom and foraminifera identification, Ar/Ar dating of hornblende, U-Pb and U-Th dating, and grain and particle size distribution and shape. During sieving, the filtrate was collected in a clean bucket, allowed to settle for 72 hours in a refrigerator, and the water decanted via suction. The samples were then frozen at -15°C and shipped to the University at Buffalo.

S2.2 Lipid biomarker analyses

Samples for lipid analysis were freeze-dried and weighed to obtain the dry sediment weight prior to extractions of the total lipid extracts (TLE). Lipid extraction was carried out using an ASE 200 Accelerated Solvent Extractor (Dionex), using 9:1 [volume/volume (v/v)] dichloromethane (DCM):methanol (MeOH) as the solvent. These ASE extractions were performed in three cycles at 120°C and 1200 psi. The TLE was weighed, and then surrogates were added: 4.2 μg of $C_{20,1}$ *n*-alkanoic acid and 0.1 μg C_{46} glycerol dialkyl glycerol tetraether (GDGT) (Huguet et al., 2006). Subsequently, the extracts were separated into different fractions using flash column chromatography: the fatty acids and neutral fractions in the TLE were separated using aminopropylsilyl as the stationary phase and 94:6 (v/v) DCM:acetic acid as the eluent for the acid fraction, while 2:1 (v/v) DCM:isopropanol (IPA) for the neutral fraction. The collected fatty acid fractions were derivatized at 60°C overnight using 5% anhydrous acetyl chloride in HPLC-grade MeOH to convert all the fatty acids into fatty acid methyl esters (FAMEs). This process makes the fatty acids amenable in gas chromatography (GC) analysis. A subsequent cleanup step was taken to remove the excess water generated as a by-product in the methylation reaction. This was done using activated silica (SiO_2) gel columns as the solid phase and the DCM as the eluent. The neutral fractions underwent further extraction to separate the apolar and polar fractions. The polar fractions contain the GDGTs. The neutral fractions were loaded to alumina column and then eluted with 9:1 hexane:DCM to collect the apolar fractions followed by elution with 1:1 (v/v) DCM:MeOH to collect the polar fractions. The collected polar fractions were dried down under nitrogen gas and reconstituted with ~250–300 μL of 99:1 hexane:IPA (v/v) and then filtered using PTFE filters prior to high-performance liquid chromatography (HPLC) analysis.

Fatty acid methyl esters (FAMEs) were analyzed on a Trace 1310 GC with flame ionization detector (FID) (Thermo Scientific) equipped with two AI 1310 autosamplers in a parallel configuration. The analysis was performed using HP-1ms fused silica columns (Agilent Technologies), with dimensions of 30 m column length, 0.250 mm inner diameter and 0.25 μm film thickness. Split/splitless injections were done at 250°C, with split flow of 14 mL/min for the first 0.75 min, and a constant column flow of 3.60 mL/min using hydrogen as the carrier gas. The GC separations were performed in a temperature gradient program with an initial temperature set at 70°C for 1 min, then increased to 230°C at 27°C/min rate, followed by a ramp to 315°C at 6°C/min with a final hold for 10 min. Peak area responses of FAMEs were normalized using the internal standard peak response and FAME concentrations were calculated using an external standard calibration using octacosanoic acid methyl ester.

The FAME hydrogen and carbon stable isotope values were analyzed using GC-high temperature conversion-isotope ratio mass spectrometry (IRMS) on a Delta V Plus IRMS connected via ConFlo IV and Isolink II to a Trace 1310 GC (Thermo Scientific). Gas chromatography conditions and temperature gradient program were the same as the GC-FID instrument setup except for the carrier gas, which was helium at a flow rate of 1.5 mL/min. All samples were injected in triplicate. Standards of known isotopic composition were used to track drift (C_{18} and C_{24} FAMEs) and linearity (C_{20} and C_{28} FAMEs). Hydrogen stable isotope values were normalized to the Vienna Standard Mean Ocean Water (VSMOW) scale, while carbon stable isotope values were normalized to the Vienna Pee Dee Belemnite (VPBD) scale. FAMEs were corrected for the δ^2H and $\delta^{13}C$ value of the added methyl group using palmitic acid of a known isotope value (Lee et al., 2017). The total uncertainty associated with the measured δ^2H and $\delta^{13}C$ values is the standard error of the mean (SEM), which includes the uncertainty in the peak-size and drift corrections, the replicate variability, and the methyl group correction. The H_3^+ factors were determined at every beginning of the IRMS sequence ranging from 2.92 ± 0.01 to 4.83 ± 0.07 ppm/nA. Difference between these values reflects measurements taken at very different times, rather than analytical inconsistency.

Filtered polar fractions were analyzed for GDGTs in the UMass Amherst Biogeochemistry Laboratory. GDGTs, including brGDGTs and isoGDGTs, were quantified with respect to the C_{46} standard, assuming equal ionization efficiency for all compounds. GDGTs were analyzed using an Agilent 1260 Ultra High-Performance Liquid Chromatograph (UHPLC) coupled to an Agilent 6120 Mass Selective Detector (MSD run in selected ion monitoring (SIM) mode for the major GDGT protonated molecules $[M + H]^+$ following the method of (Hopmans et al., 2016), which separates the 5-methyl and 6-methyl brGDGT isomers. This method utilizes two Waters BEH HILIC silica columns (2.1 x 150 mm, 1.7 µm) in series with a Waters 2.1 x 5 mm pre-column of the same material (Hopmans et al., 2016). A gradient mobile phase involving A (hexane) and mobile phase B (hexane:IPA (v/v)) was used. Chromatographic separation was first done with isocratic elution for the first 25 min using 18% mobile phase B, then a linear increase to 35% in 25 min, and finally a linear gradient to 100% in 30 min (Hopmans et al., 2016). The flow rate was 0.2 mL/min and temperature was held constant at 30°C.

S2.3 Compilation of Modern Temperature and Isotope Data

To establish modern reference values for each study site, we compiled temperature and precipitation isotope values. Tables S1 and S2 summarize site metadata, including latitude, longitude, elevation, and the time period used to define modern conditions for each site, providing a clear reference against which paleoclimate datasets are compared. We strove to use the same reference period for all sites, wherever possible. Modern temperature values were derived from ERA5 Climate Reanalyzer data sets spanning 1950–2000 (Hersbach et al., 2020), except for ice-core sites, for which modern temperature estimates were taken directly from the datasets provided in the original ice-core studies (Buizert et al., 2018; Kobashi et al., 2017). Modern isotope values were obtained using the Online Isotopes in Precipitation Calculator (OIPC) (Bowen, 2017; Bowen et al., 2005), which is based on data from Global Network of

Isotopes in Precipitation (GNIP) (IAEA/WMO, 2015) and reflects the time period 1960–2017, except for the ice core sites, where modern isotope values were adopted from datasets reported in the original ice-core studies (Andersen et al., 2004; Dahl-Jensen et al., 2013; Dansgaard et al., 1982; Dansgaard et al., 1969; Grootes & Stuiver, 1999; Johnsen et al., 1997; Schüpbach et al., 2018; Vinther et al., 2009). Although the time periods used to define modern conditions for ice-core sites vary among studies, they fall within or overlap the broader modern intervals defined by the ERA5 and GNIP/OIPC datasets, ensuring consistency and comparability across sites.

Text S3. Results

S3.1 GDGT results and choice of temperature calibration

Both brGDGTs and isoGDGTs are present in all samples that were analyzed. brGDGTs were an order of magnitude higher concentration than isoGDGTs (Figure S3). Total brGDGT concentrations ranged from 0.06 to 0.83 µg/g dry sediment with the lower layer having the lowest concentrations (Figure S3A). Unit 5 of the core showed the highest concentrations of brGDGTs ranging from 0.25 to 0.83 µg/g dry sediment. Total isoGDGT concentrations ranged from 0.002 to 0.019 µg/g dry sediment. The total isoGDGT concentration increased down-core (Figure S3B).

The most abundant brGDGT is IIIa (median fractional abundance = 0.40 ± 0.05), then IIa (median fractional abundance = 0.22 ± 0.05) followed by IIa′, Ia and IIIa′ with almost the same median fractional abundance of 0.10 ± 0.03 (Figure S2). Acyclic brGDGTs (92%) are more abundant than the brGDGTs with cyclopentane moieties (8%). brGDGTs with 5-methyl isomers are more abundant than 6-methyl isomers, with total percentages of 78% and 22%, respectively (Figure S2). Hexamethyl brGDGTs (51%) are most abundant, followed by pentamethyl (37%) and tetramethyl (22%) (Figure S2).

Caldarchaeol (GDGT-0) and crenarchaeol (GDGT-4) are the most abundant isoGDGTs, with median fractional abundances of 0.72 ± 0.06 and 0.17 ± 0.05, respectively. The ratio of caldarchaeol to crenarchaeol (Blaga et al., 2009) ranges from 2.18 to 7.67, with the highest values in Unit 5 except for the topmost sample (Figure S3E). The crenarchaeol regioisomer (GDGT-4′) is not detected in all the samples, hence we did not apply the TEX_{86} paleothermometer (Schouten et al., 2013). The branched to isoprenoid tetraether ratio (BIT) is above 0.96 for the entire core (Figure S3F).

The MBT'_{5Me} index ranges from 0.15 to 0.28 (Figure S3D). Unit 1 showed relatively stable values. Unit 3 had high values followed by a decreasing trend to units 4 and 5, and then a sudden increase in the topmost sample in Unit 5, which has the highest value. The topmost samples in Unit 2 have comparable values with the MBT'_{5Me} values in Unit 3, while the lower samples in Unit 2 have similar values to those in Unit 1. Unit 1 samples have consistent values and demonstrated the lowest MBT'_{5Me} compared to the other units (Figure S3D). Fractional abundances of hexamethylated brGDGTs are higher in Unit 1 compared to the upper Units 305. (Figure S3C). The CBT_{5Me} index ranges from 1.72 to 3.01 and is mirrored by the fC index.

Higher CBT_{5Me} index values were observed in the upper units compared to the lower units. The highest CBT_{5Me} index values were observed in Units 3–4 and the topmost sample in Unit 5 (Figure S3G). The isomer ratio (IR) index ranges from 0.15 to 0.29, with relatively high and consistent values in Unit 1 (Figure S3I).

We compared the MBT'_{5Me} index values from Camp Century with those from the warmest two millennia between 11.7 to 5.0 ka from Greenland lake time series (Fig. S4). This comparison provides an estimate of the magnitude of temperature difference from modern. Using this index for comparison rather than temperature calibrations allows for a direct assessment of biomarker signals across sites without introducing uncertainties associated with calibration choice. We compared the MBT'_{5Me} values to modern temperature (right y-axis in Fig. S4) at each location and estimate MBT'_{5Me} values from modern temperature using the MBT'_{5Me}-temperature calibration (Otiniano et al., 2024). This provides a measure of the magnitude of difference between the temperature recorded by GDGTs and the modern temperature at each location. Camp Century MBT'_{5Me} values are clustered between 0.15–0.25, whereas the lake data display higher MBT'_{5Me} values, consistent with warmer conditions.

To estimate air temperatures during months above freezing (MAF) from the Camp Century brGDGTs, we applied two high-latitude lake-based calibrations (Otiniano et al., 2024; Raberg et al., 2021) (Equations S1 and S2, Figure S4). These calibrations were selected because they were developed from Arctic Lake datasets, where brGDGT distributions show the strongest sensitivity to mean MAF temperatures (Equations S1 and S2). Other commonly used calibrations target mean annual air temperature or summer lake water temperature and are based on lower-latitude or soil-derived GDGT assemblages, making them less suitable for the Camp Century site. One available brGDGT calibration (Otiniano et al., 2023) was developed mainly from Alaska and northern America sites and may not reflect Greenland conditions, so we applied calibration derived from high-latitude Arctic lakes instead (Otiniano et al., 2024; Raberg et al., 2021)

Equation S1:

$$MAF\ Temperature\ (°C)_{RabergFull} = -8.06 + 37.52fIa - 266.83fIb^2 + 133.42fIb + 100.85fIIa'^2 + 58.15fIIIa'^2 + 12.79fIIIa$$

Equation S2:

$$MAF\ Temperature\ (°C)_{Otiniano2024} = 17.0 - 11.4fIIa - 17.4fIIIa - 15.9fIIa' - 124.4fIIIb$$

S3.2 Leaf wax distribution and isotope composition

We calculated the average chain length (ACL) of *n*-alkanoic acid leaf waxes to assess possible changes in vegetation and plant sources (Equation S3, Figure S6D). All samples from all units contain C_{20} to C_{32} *n*-alkanoic acids with a carbon preference index (CPI) exceeding 2.10 (Equation S4, Figure S6E). In the upper section of the core, which includes Units 3–5, there are higher concentrations of *n*-alkanoic acids per gram of dry sediment when compared to Unit 1, which exhibited consistently low concentration. Relatively high concentrations of the *n*-alkanoic acids were consistently observed in Unit 2 (Figure S6A). C_{24} *n*-alkanoic acids dominate Units 2–

5, while Unit 1 shows similar abundances of C_{24}, C_{26}, and C_{28} (27–31%). Mid-chain *n*-alkanoic acids (C_{20}–C_{24}) are most abundant in Unit 2, and longer chains (C_{26}–C_{30}) are more prevalent in Unit 1.

Equation S3:

$$ACL_{C_{20}-C_{30}} = \frac{(20\ x\ C_{20}) + (22\ x\ C_{22}) + (24\ x\ C_{24}) + (26\ x\ C_{26}) + (28\ x\ C_{28}) + (30\ x\ C_{30})}{C_{20} + C_{22} + C_{24} + C_{26} + C_{28} + C_{30}}$$

Equation S4:

$$CPI_{C_{20}-C_{32}} = \frac{1}{2}\left(\left(\frac{C_{20} + C_{22} + C_{24} + C_{26} + C_{28} + C_{30}}{C_{21} + C_{23} + C_{25} + C_{27} + C_{29} + C_{31}}\right) + \left(\frac{C_{22} + C_{24} + C_{26} + C_{28} + C_{30} + C_{32}}{C_{21} + C_{23} + C_{25} + C_{27} + C_{29} + C_{31}}\right)\right)$$

Carbon isotope values ($\delta^{13}C$) for even chain C_{20}–C_{30} *n*-alkanoic acids were measured for each core segment. The results from C_{32} *n*-alkanoic acids were excluded since the peaks were lower than the detection limits of the IRMS. In the upper units (Unit 3–5), mid-chain lengths (C_{20}–C_{22}) have similar patterns, while longer chain lengths (C_{26}–C_{30}) exhibit a pattern distinct from the mid-chain compounds, but similar patterns to each other (Figure S6C, Figure S8). C_{30} showed the most depleted ^{13}C values. In unit 2, all the chain lengths showed the same $\delta^{13}C$ profile. As in the upper 3 units, long- and mid-chain waxes have distinct $\delta^{13}C$ patterns in Unit 1. We compared the $\delta^{13}C$ values with modern $\delta^{13}C$ distributions of plant waxes of different vegetation sources (Hollister et al., 2022). Longer chain lengths (C_{26}–C_{28}) have $\delta^{13}C$ values that partly overlap with the range of graminoids but fall entirely within the range characteristic of shrubs (Figure S7). For C_{22} *n*-alkanoic acid, $\delta^{13}C$ values in Units 2–5 mostly fall within the ranges of graminoids and shrubs, while in Unit 1, some samples also fall within the graminoid and shrub range, and others have lower $\delta^{13}C$ values consistent with aquatic moss (Figure S7).

The $\delta^{2}H$ for even-chain *n*-alkanoic acid from C_{20}–C_{30} were analyzed in each sample. C_{32} waxes were excluded since the peak responses were lower than the detection limits of the instrument. For Unit 1, C_{22} and C_{24} shared a similar pattern, as did C_{26} and C_{28}. C_{20} showed a similar trend to C_{22} and C_{24} but has more ^{2}H-depleted values. In general, $\delta^{2}H$ values in Unit 2 are ^{2}H-enriched compared to other units. In the upper units, C_{20} and C_{22} exhibited similar patterns and showed the most ^{2}H-depleted values. In contrast, C_{24}, C_{26} and C_{28} have comparable values and trends with significantly ^{2}H-enriched values compared to C_{20} and C_{22}. C_{30} is the most ^{2}H-enriched and follows a distinct trend compared to the other chain length homologues (Figure S6C).

S3.3 Determining Camp Century paleo-elevation

Because the Greenland Ice Sheet has undergone significant loading and unloading through past glacial–interglacial cycles, it is necessary to adjust elevations when interpreting sedimentary archives to account for glacial isostatic deformation. The ice sheet's massive weight depresses the underlying crust, so past ice retreat or hypothetical removal would cause isostatic uplift of the bedrock, making such adjustments essential for accurate paleo-surface reconstructions (Paxman et al., 2022). We applied an elevation adjustment for solid Earth

subsidence caused by ice sheet loading, using reconstructed total isostatic deformation values to estimate vertical displacement at Camp Century. From the four grid cells nearest the site, the fully adjusted elevation was 280 ± 50 m (Paxman et al., 2022). Modern bedrock elevation of 530 ± 30 m was obtained by getting the average of elevation values of the four grid cells nearest the site from the BedMachine topography dataset (Morlighem et al., 2017). Combining these values yields a fully adjusted paleo-elevation of 810 ± 60 m for the Camp Century site. While these corrections improve confidence in our reconstructions, uncertainties remain, particularly in relation to forebulge dynamics and spatial variability in Earth structure, which may not be fully captured in the regional isostatic models.

S3.4 Modern elevation-adjusted stable water isotope and temperature values at Camp Century

Modern (1950–2000 CE) temperature values were obtained from Pituffik station (Hersbach et al., 2020) at 77 m asl and scaled to Camp Century paleo-elevation (810 ± 60 m) using mean monthly (June, July, August) slope lapse rates, which are empirically constrained gradients across Greenland (Fausto et al., 2009) (Equation S5). Modern precipitation isotope values (1966–1969) were also obtained from the Pituffik station (IAEA/WMO, 2015) and corrected to the paleo-elevation at Camp Century using stable water isotope lapse rates appropriate for high-latitude settings. Stable water isotope lapse rates are based on empirical relationships between precipitation isotopes and elevation with quantitative elevation-isotope gradients and associated uncertainties constrained by global syntheses of isotope-elevation relationships (Dansgaard, 1964; Poage & Chamberlain, 2001) (Equation S6). We used a high-latitude, low-elevation lapse rate for summer precipitation of -46 ± 8‰ for δ^2H from Koerner & Russell (1979) that spans ~1 km elevation change. Uncertainties for the modern elevation-adjusted temperature and precipitation isotope values for Camp Century were estimated by propagating uncertainties in the fully adjusted elevation, the slope lapse rates, and the standard error of the mean (SEM) of the corrected values. We calculated the mean across all months with temperatures above freezing after elevation correction, ensuring regional consistency with MAF estimates and the standard approach for calculating mean summer precipitation isotopes.

Equation S5:

$$T_{CampCentury} = T_{Pituffik} - \Gamma * (h_{CampCentury} - h_{Pituffik})$$

Equation S6:

$$\delta^2H_{CampCentury} = \delta^2H_{Pituffik} - \Gamma * (h_{CampCentury} - h_{Pituffik})$$

S3.5 δ^2H_{C22} as a proxy for summer precipitation δ^2H and δ^2H_{C28} as a proxy for summer precipitation δ^2H and evaporation enrichment

Long-chain *n*-alkanoic acids (≥C_{26}) are typically associated with terrestrial plants such as Arctic shrubs and mosses (Cowling et al., 2022; Dion-Kirschner et al., 2020; Sachse et al., 2012; Thomas et al., 2016), whereas mid-chain compounds (≤C_{24}) are more abundant in aquatic plants and algae (Berke et al., 2019; Gao et al., 2011; Thomas et al., 2020), but C_{24} is also dominant in Arctic shrubs (Hollister et al., 2022), so this compound may reflect mixed

sources. Macrofossil evidence from the site, including twigs, mosses, and woody tissues, further confirms that a variety of vegetation similar to the bioclimate zone at Pituffik today, including mosses like *Tomentypnum nitens* and *Polytrichum juniperinum*, existed in the region during ice-free periods (Christ et al., 2021).

Leaf wax δ^2H values reflect the δ^2H values of the source water that were taken up by the plants, with additional impacts of evaporative ^2H-enrichment of leaf water and biosynthetic fractionation (Sachse et al., 2012). Terrestrial plants use soil water, which primarily reflects the δ^2H values of summer precipitation, as most precipitation occurs during this season and active layer water is recharged by summer precipitation (Gorbey et al., 2022; Thomas et al., 2020). The isotope composition of the leaf water can vary markedly from that of the plant's source water. This is the result of transpiration, or water loss from the leaf, where the lighter water isotopes evaporate and diffuse in air faster than the heavier ones (Sachse et al., 2012). During the synthesis of leaf wax lipids, a biosynthetic fractionation occurs that imparts a consistent offset between the δ^2H of the leaf water and the resulting leaf waxes. The resulting leaf wax δ^2H values thus reflect a combination of summer precipitation δ^2H, the extent of evaporative enrichment of leaf water, and the intrinsic biosynthetic fractionation during lipid formation.

Aquatic plant δ^2H values closely reflect lake water δ^2H, as these plants absorb water directly from their environment with minimal evaporative enrichment compared to terrestrial plants (Sachse et al., 2012). During lipid biosynthesis, an apparent fractionation occurs between the hydrogen isotope composition of source water and that of the resulting leaf wax lipids. In Arctic lakes and streams, aquatic plant wax δ^2H primarily records summer water δ^2H because lipids are produced during the short growing season when temperatures are above freezing. Evaporation is minimal, especially early during the ice-free season, when leaf flush occurs, so the δ^2H of lake water used by aquatic plants reflects the isotope composition of summer precipitation. We converted leaf wax hydrogen isotope values to source water isotope values using published modern plant fractionation data (Equations S7 and S8). For mid-chain aquatic plant waxes, we estimated the δ^2H of lake water by compiling published apparent hydrogen isotope fractionation values between lake water and submerged plant leaf wax δ^2H (ε_{app}), yielding a mean of -124 ± 5‰ (n=13) (Dion-Kirschner et al., 2020; Gorbey et al., 2022; Hollister et al., 2022). For long-chain terrestrial plant waxes (C_{28} δ^2H), we inferred leaf water δ^2H values using the biosynthetic hydrogen isotope fractionation (ε_{bio}) value of -143 ± 5‰ (n=13) compiled from studies that published isotope values for leaf waxes and leaf water at high-latitude sites (O'Connor et al., 2020). We chose ε_{bio} to estimate leaf water δ^2H rather than using the apparent fractionation (ε_{app}) between source water δ^2H and leaf wax δ^2H, as ε_{app} assumes constant evaporative enrichment and is therefore less effective at capturing changes in evapotranspiration over time.

We calculate the difference between lake and leaf water δ^2H, which reflects the degree of evaporative ^2H-enrichment, since both leaf and lake water sources are summer precipitation δ^2H (Equation S9).

Equation S7:

$$\delta^2 H_{LakeWater} = \left(\frac{1000 + \delta^2 H_{PlantWax(C_{23}\ or\ C_{24}\ or\ C_{25})}}{\left(\frac{\varepsilon_{LakeWater(C_{23}\ or\ C_{24}\ or\ C_{25})}}{1000}\right) + 1} \right) - 1000$$

Equations S8:

$$\delta^2 H_{LeafWater} = \left(\frac{1000 + \delta^2 H_{PlantWax(C_{28}\ or\ C_{29})}}{\left(\frac{\varepsilon_{LakeWater(C_{28}\ or\ C_{29})}}{1000}\right) + 1} \right) - 1000$$

Equation S9:

$$\varepsilon_{Leaf-Lake} = \left(\frac{1000 + \delta^2 H_{LeafWater}}{\left(1000 + \delta^2 H_{LakeWater)}\right) - 1} \right) * 1000$$

S3.6 Comparison of Camp Century values with other datasets in Greenland

To evaluate Camp Century reconstructions alongside other Greenland datasets, we constructed anomaly plots for brGDGT-inferred MAF temperatures, summer δ^2H precipitation, and leaf water δ^2H, each calculated relative to modern observations (Table S1 & S2). For all comparisons, consistent calibrations were applied across sites, and uncertainties were estimated by propagating errors from modern observations, variability within each time series, and calibration RMSE. In each individual temperature time series, only the values during the warmest two millennia between 11.7–5.0 ka were selected to capture maximum Holocene warmth**.** For isotope datasets, some records lack temperature constraints, we therefore selected values from the middle Holocene (8–5 ka), corresponding to a period typically associated with peak Holocene warmth (Axford et al., 2021; Briner et al., 2016).

We compared the mean brGDGT-inferred MAF temperature at Camp Century with brGDGT-inferred MAF temperature using the same brGDGT-temperature calibrations in the following lake sediment archives: 578, Bullet, Marshall, Rosaea, Gus, N3, Pluto and Sikuiui (Acharya et al., 2025; Cluett et al., 2023; Otiniano et al., 2024; Raberg et al., 2021; Schneider et al., 2024; Thomas et al., 2018). Additional temperature reconstructions included mean annual air temperature from argon and nitrogen isotopes in ice cores (Kobashi et al., 2017; Martin et al., 2024), summer air temperature inferred from ice-core data assimilation (Buizert et al., 2018), and July air temperature from chironomid assemblages (Axford et al., 2019; Axford et al., 2017; Axford et al., 2013; McFarlin et al., 2018). Camp Century MAF values were also compared with one chironomid-based July air temperature dataset from the Last Interglacial (LIG) (McFarlin et al., 2018)) and with July air temperatures inferred from macrofossils dating to the LIG and the Early Pleistocene and Plio-Pleistocene (Atti et al., 2024; Bennike, 1990; Bennike et al., 2002; Bennike & Böcher, 1992, 1994; Bennike et al., 2023; Bennike et al., 2010; Brodersen & Bennike, 2003; Hedenäs, 1994; Hedenäs & Bennike, 2003).

Summer δ^2H precipitation values were compared with leaf-wax δ^2H data from Flower Valley Lake and Pluto Lake (Balascio et al., 2013; Thomas et al., 2020) using mean ε_{app} values derived from submerged and floating aquatic plants in high-latitude sites (Dion-Kirschner et al., 2020; Gorbey et al., 2022; Hollister et al., 2022) to reconstruct source water δ^2H (Equation S7). For Flower Valley Lake, we used C_{25} δ^2H as mid-chain aquatic plant wax and converted into

lake water δ^2H using the mean ε_{app} value of -132 ± 5‰ (n=15); For Pluto Lake, we used C_{22} δ^2H and converted into lake water δ^2H using the mean ε_{app} value of -124 ± 5‰ (n=13). Additional comparisons included annual $\delta^{18}O$ from ice cores (Andersen et al., 2004; Dahl-Jensen et al., 2013; Dansgaard et al., 1982; Dansgaard et al., 1969; Grootes & Stuiver, 1997; Johnsen et al., 1997; Schüpbach et al., 2018; Stuiver & Grootes, 2000; Vinther et al., 2009) and summer $\delta^{18}O$ from moss cellulose (Lasher et al., 2017).

Leaf water δ^2H values at Camp Century were compared with Greenland Holocene leaf-water δ^2H values inferred from lake archives (Balascio et al., 2013; McFarlin et al., 2023; Thomas et al., 2020), as well as with peak interglacial leaf water δ^2H values from three interglacial periods (Marine Isotope Stages (MIS) 1, 5, and 11) at ODP Site 646 (Cluett & Thomas, 2021) reconstructed using mean ε_{bio} value between compiled leaf waxes and leaf water (Gao et al., 2014; Nichols et al., 2010; O'Connor et al., 2020) (Equation S8). To account for spatial variability in vegetation composition, region-specific ε_{bio} values were calculated based on dominant vegetation types. The ε_{bio} for each region was calculated based on the dominant vegetation types using modern Arctic vegetation maps (CAVM Team, 2024; Raynolds et al., 2019) and studies of past plant communities in these or nearby lakes (Bennike, 2000; Kusch et al., 2019) (Equation S10-12). To ensure reproducibility, Table S3 and S4 lists the leaf-water ε (epsilon) values for high-latitude sites (>50°N), including the vegetation composition for each location. Cold regions are dominated by mosses with minimal vascular plants, whereas warmer regions have higher proportions of vascular plants.

Equation S10:

$$\varepsilon_{LeafWater(C_{28})}(cold\ region) = (0.98 * \varepsilon_{Moss}) + (0.02 * \varepsilon_{MeanVascularPlants})$$

Equation S11:

$$\varepsilon_{LeafWater(C_{29})}(cold\ region) = (0.98 * \varepsilon_{Moss}) + (0.01 * \varepsilon_{Shrubs}) + (0.01 * \varepsilon_{Forbs})$$

Equation S12:

$$\varepsilon_{LeafWater(C_{28}/C_{29})}(warmer\ region) = (0.75 * \varepsilon_{Moss}) + (0.25 * \varepsilon_{MeanVascularPlants})$$

S3.7 Effect of temperature on precipitation δ^2H

The stable isotope value of atmospheric water vapor arriving at a given location is a function of the moisture source and transport history (Cluett, 2021; Gimeno et al., 2021). During condensation, the stable water isotope composition is further modified via fractionation that, under equilibrium conditions, is temperature dependent (Clark & Fritz, 1997; Majoube, 1971). To examine upstream atmospheric circulation changes at Camp Century independent from temperature change (e.g., moisture source and transport pathways), we removed the effect of local summer temperature from δ^2H precipitation, as follows. Using the brGDGT-inferred summer temperature at Camp Century, we calculated the temperature-dependent fractionation of condensation using empirically derived constants (Clark & Fritz, 1997; Majoube, 1971) (Equation S13). This assumes that the mean MAF air temperature approximates the temperature at which precipitation is condensing, and that precipitation is condensing under equilibrium conditions. Although there are issues with those assumptions, we cannot place further constraints with the data we have. We then used this temperature-dependent fractionation factor together with the mid-chain plant-wax inferred summer precipitation δ^2H

value to estimate the δ^2H value of the vapor arriving at the study site (Equation S14). We applied the same approach to the Flower Valley, Pluto, and Secret Lake data (Balascio et al., 2013; Lasher et al., 2017; Thomas et al., 2020), and to ice core time series, except that we used different empirical constants to calculate the fractionation factor for ice core data, as condensation occurs at below-freezing temperatures (Ellehoj et al., 2013). For lake time series lacking inferred temperatures, we used nearby sites: inferred temperatures from Last Chance Lake and Delta Sø were applied to Flower Valley Lake and Secret Lake, respectively. We applied the same approach to modern observations, calculating the temperature-dependent fractionation factor using ERA5 temperature from 1950–2000 CE (Hersbach et al., 2020) and GNIP- or OIPC-derived modern precipitation isotope values (Bowen, 2017; Bowen et al., 2005; IAEA/WMO, 2015) (described in detail in Text S3.6) to estimate the modern vapor δ^2H. The isotope anomaly was then determined by subtracting the modern vapor δ^2H from the paleo-vapor δ^2H estimate.

Equation S13:

$$\alpha_{(water-vapor)} = \frac{e^{\left(a\left(\frac{10^6}{T_K^2}\right)+b\left(\frac{10^3}{T_K}\right)+c\right)}}{1000}$$

Equation S14:

$$\delta_{vapor} = \left(\frac{(1000 + \delta^2 H_{LakeWater})}{\alpha_{(water-vapor)}}\right) - 1000$$

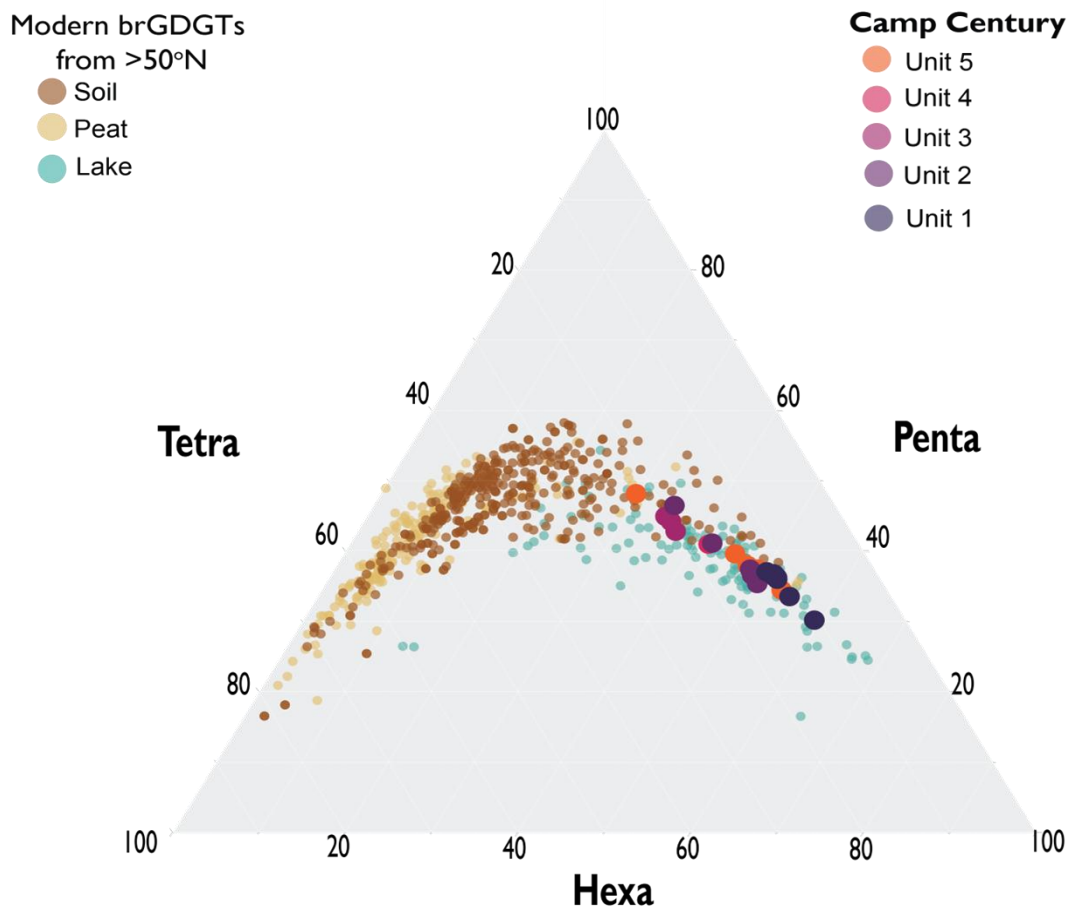

Figure S1. Ternary diagram of brGDGTs at Camp Century, large dots colored by different stratigraphic units, compared to brGDGTs from modern soil, peat and lake sources in high-latitude areas (Cluett et al., 2023; Lindberg et al., 2022; Martínez-Sosa et al., 2021; Naafs et al., 2017; Raberg et al., 2021; Russell et al., 2018; Thomas et al., 2018; Zhao et al., 2023). Tetra: tetramethylated brGDGTs, penta: pentamethylated brGDGTs, hexa: hexamethylated brGDGTs. GDGTs are numbered as in Hopmans et al. (2016) and De Jonge et al. (2014).

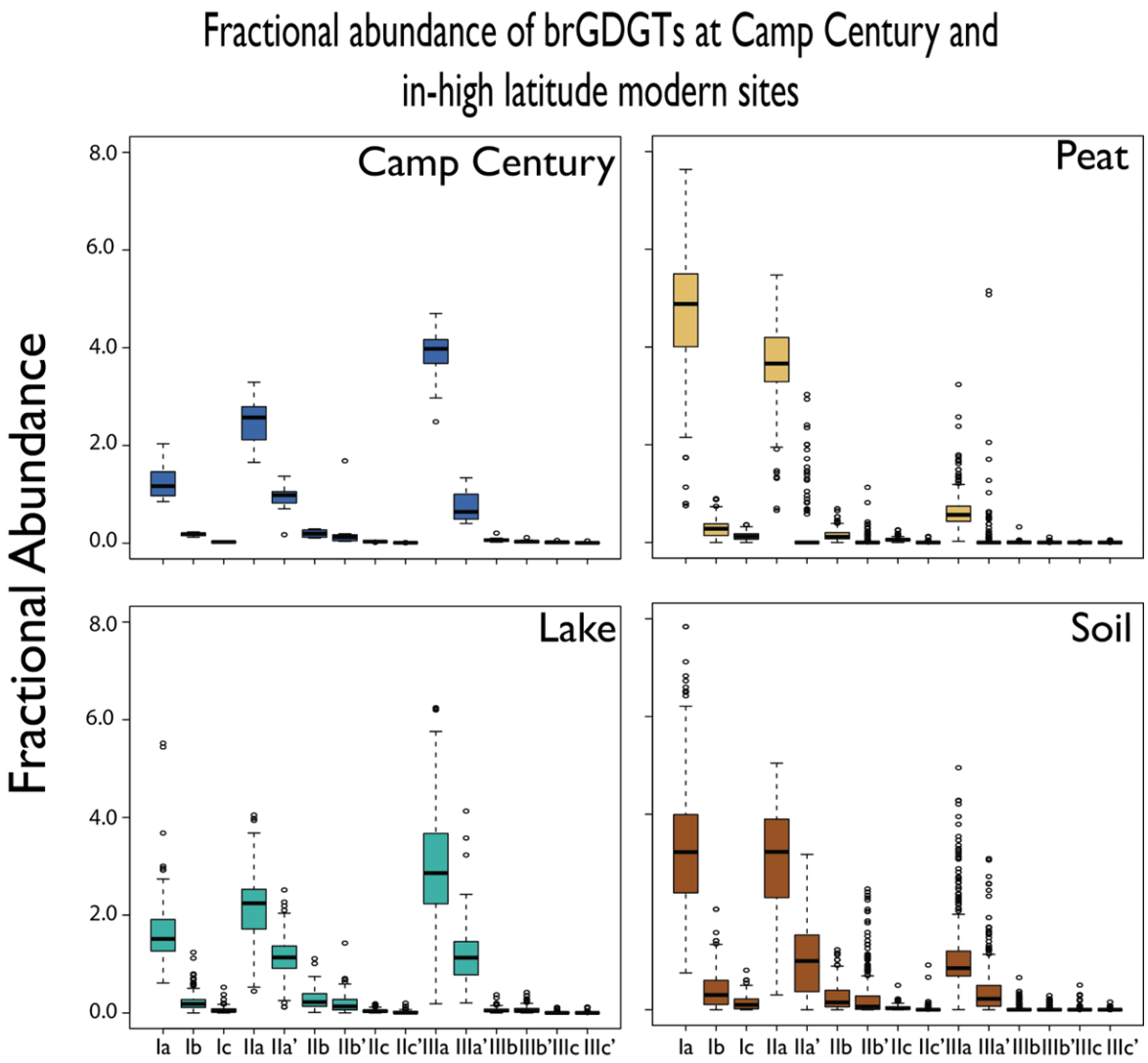

Figure S2. Fractional abundance of brGDGTs at Camp Century and modern brGDGTs in high-latitude areas. Box plots: bold lines: median, boxes: interquartile range, whiskers: 5th and 95th percentiles, dots: outliers. (Cluett et al., 2023; Lindberg et al., 2022; Martínez-Sosa et al., 2021; Naafs et al., 2017; Raberg et al., 2021; Russell et al., 2018; Thomas et al., 2018; Zhao et al., 2023).GDGTs are numbered as in Hopmans et al. (2016) and De Jonge et al. (2014). GDGTs are numbered as in Hopmans et al. (2016) and De Jonge et al. (2014).

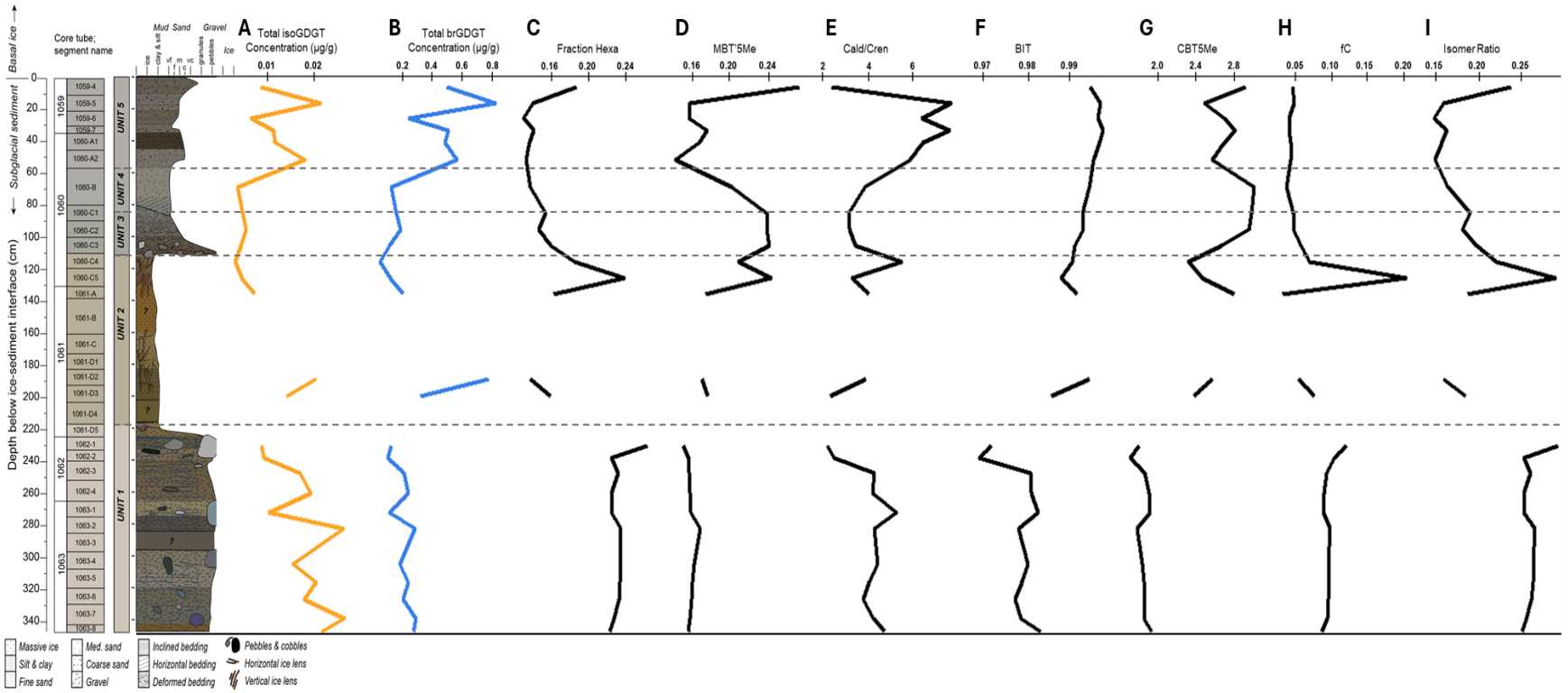

Figure S3. Downcore pattern of GDGTs and their indices in Camp Century, northwestern Greenland. (A) Concentrations of total isoprenoid (iso) GDGTs. (B) Concentrations of total branched (br) GDGTs. (C) Fractional abundance of hexamethylated brGDGTs. (D) MBT'_{5Me} index. (E) Ratio of caldarchaeol to crenarchaeol (Blaga et al., 2009). (F) Ratio of branched to isoprenoid tetraether (G) CBT_{5Me} index. (H) fC index. (I) Isomer Ratio.

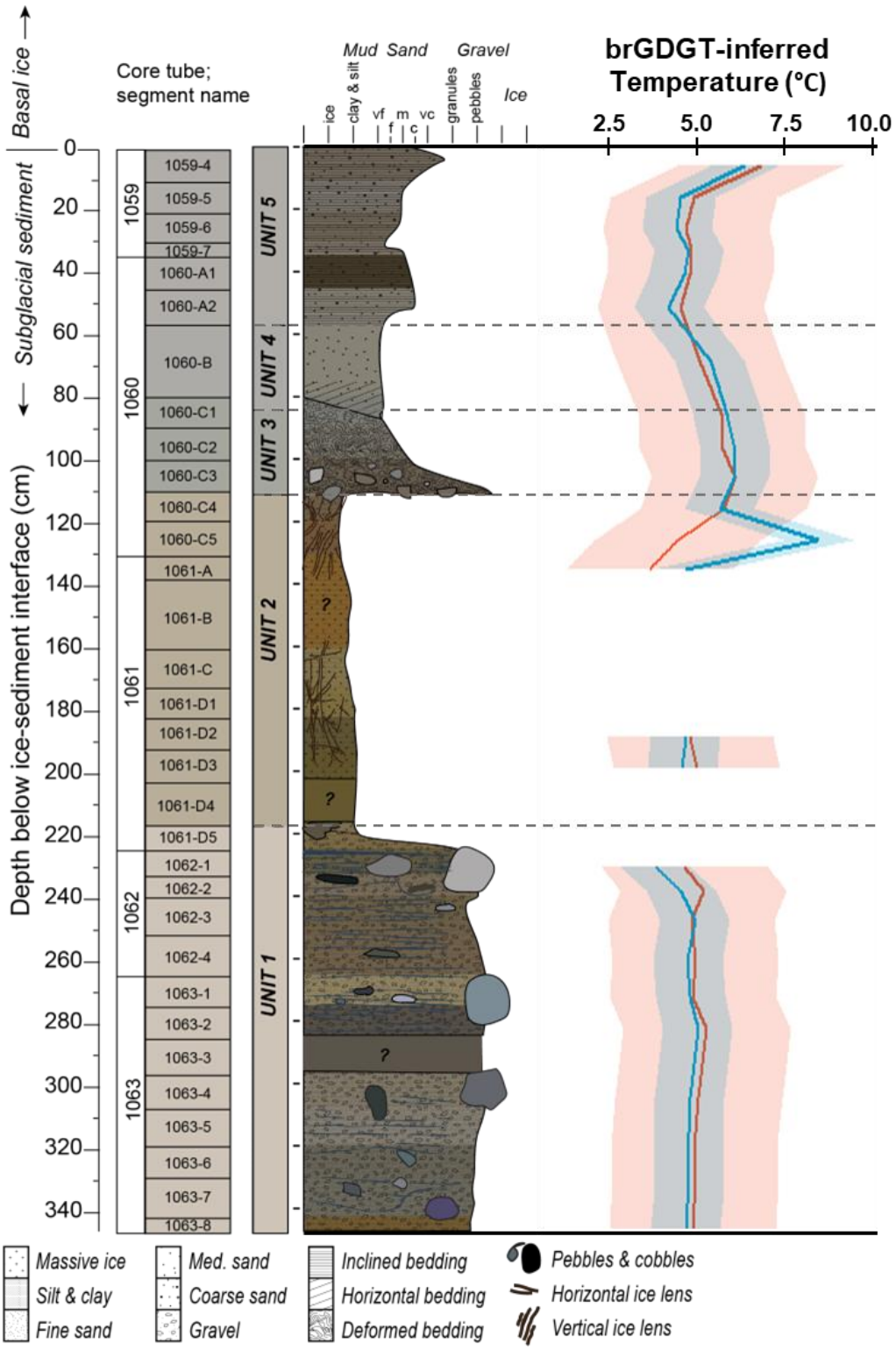

Figure S4. Reconstructed months above freezing (MAF) temperatures in Camp Century, northwestern Greenland using Raberg et al., (2021) (red), and Otiniano et al., (2024) (blue). Missing points indicate samples with GDGT abundances below instrumental detection limits. Shading indicates uncertainties associated with the temperature calibration errors.

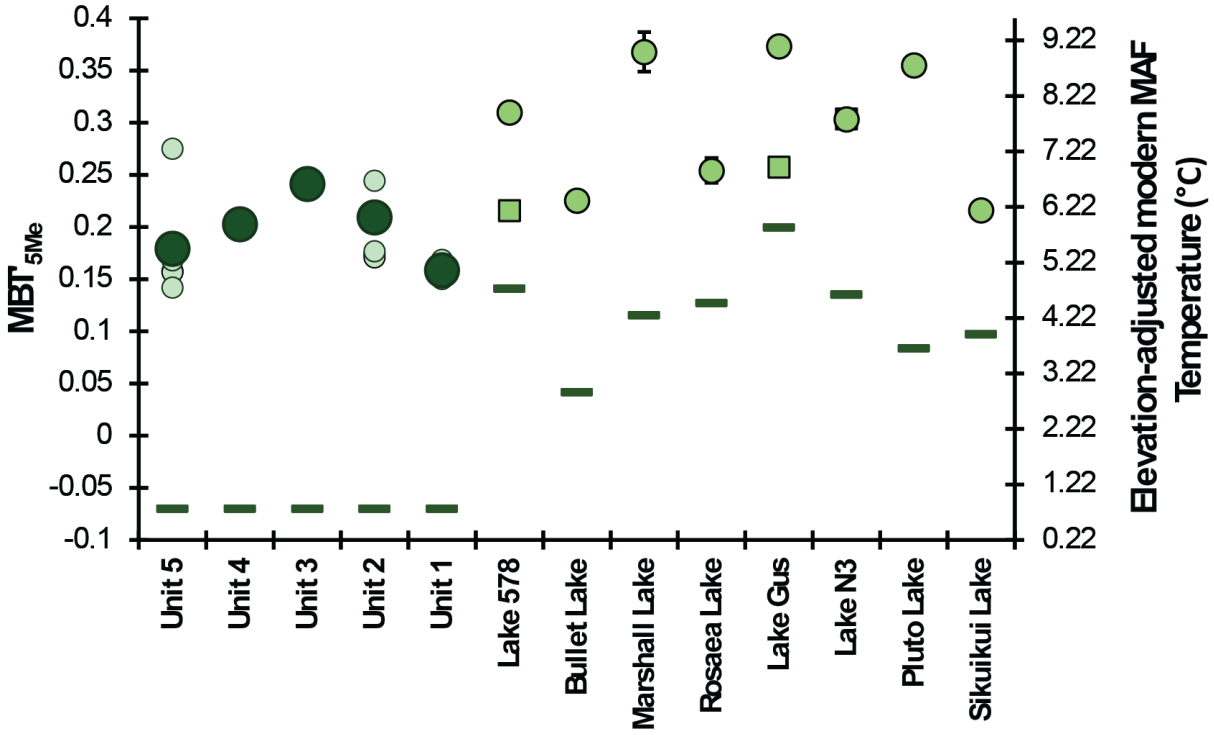

Figure S5. MBT′$_{5Me}$ distributions in Camp Century units and in western Greenland Holocene Lake sediments (circles and squares; left y-axis), compared to modern months above freezing (MAF) temperature (lines; right y-axis). A: Camp Century MBT′$_{5Me}$ values and temperature. Light green circles: individual samples; dark green circles: mean value for each Unit, dark green line: modern MAF temperature. Uncertainties include standard error of the mean (SEM) of each sample; all error bars are smaller than the plotted symbols. B: MBT′$_{5Me}$ distributions in western Greenland Holocene Lake sediments (Acharya et al., 2025; Cluett et al., 2023; Schneider et al., 2024; Thomas et al., 2018). Circle: mean values spanning the warmest two millennia from 11.7 to 5 ka, square: mean value of the late 20th century sample from each lake dataset (not available for Bullet Lake, Marshall Lake, Rosaea Lake, Pluto Lake, and Sikuiui Lake), dark green line: modern MAF temperature at these sites. The y-axis scales are directly calculated from one another using the MBT′$_{5Me}$-temperature calibration (Otiniano et al., 2024).

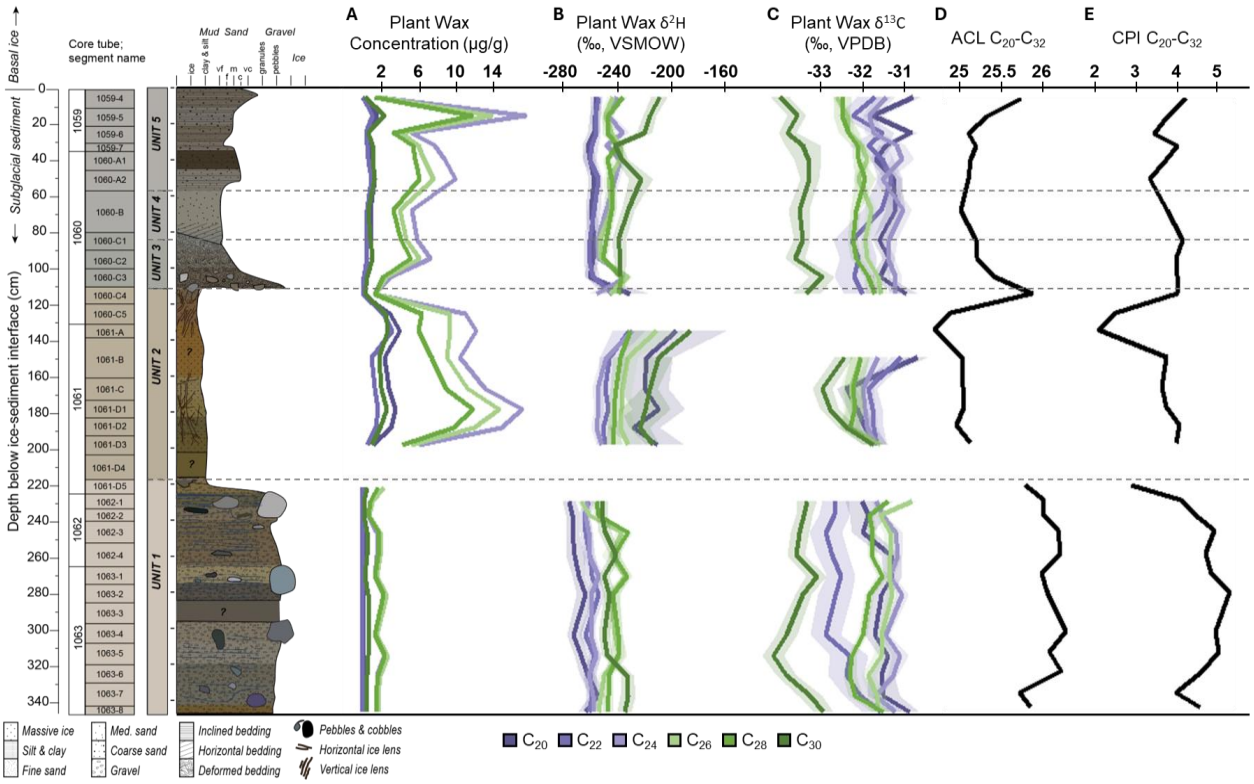

Figure S6. Down core plant wax data from Camp Century, northwestern Greenland. (A) Concentration of C_{20} to C_{30} *n*-alkanoic acids. (B–C) $\delta^{13}C$ and $\delta^{2}H$ of C_{20} to C_{30} *n*-alkanoic acids. (D) Average chain length (ACL) of even-chain *n*-alkanoic acids (C_{20}–C_{32}). (E) Carbon preference index (CPI) for *n*-alkanoic acids (C_{20}–C_{32}). Shading in B and C is the total uncertainty associated with the measured $\delta^{2}H$ and $\delta^{13}C$ values is the standard error of the mean (SEM), which includes the uncertainty in the peak-size and drift corrections, the replicate variability, and the methyl group correction.

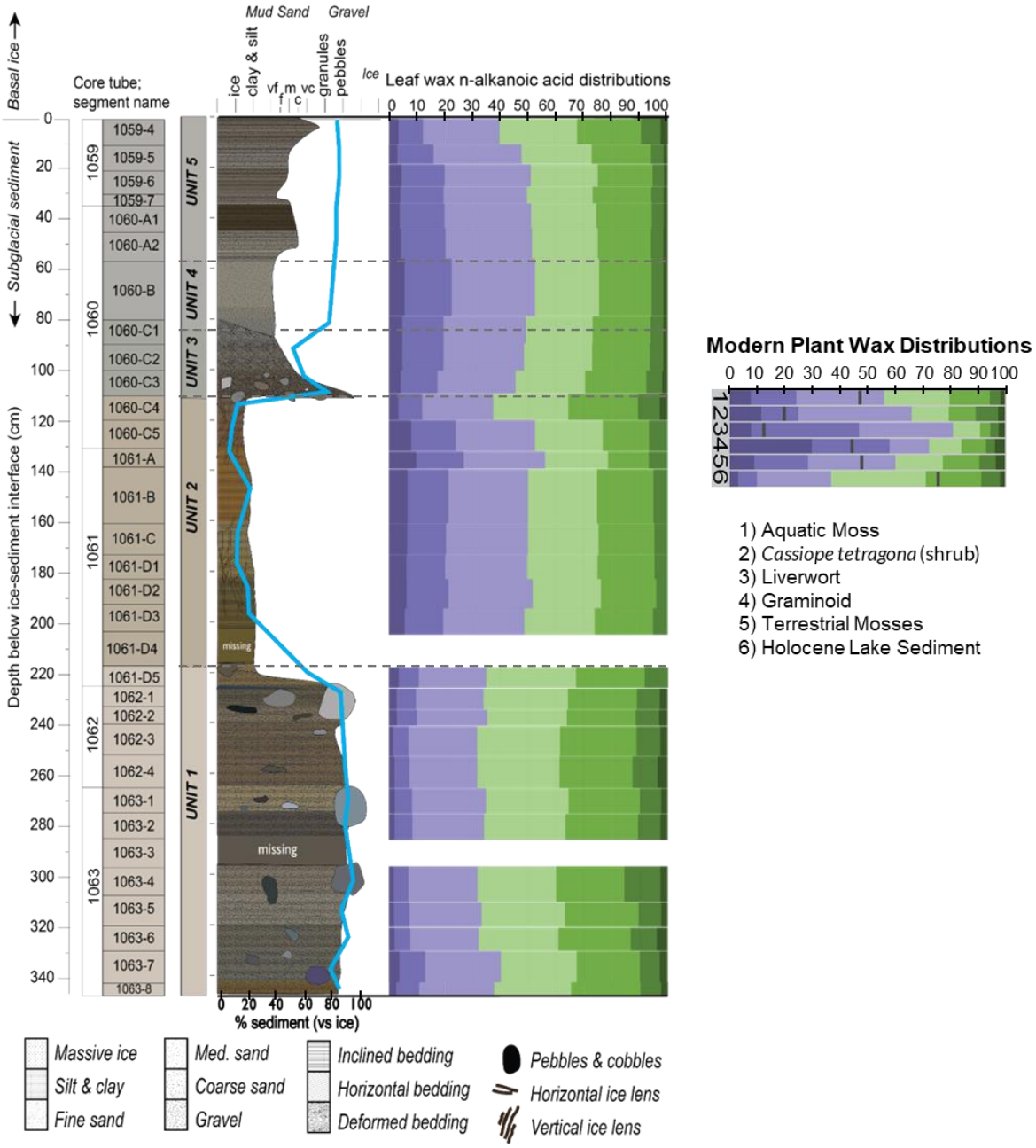

Figure S7. Downcore fractional abundance of *n*-alkanoic acid chain lengths compared with modern and Greenland Holocene Lake sediment plant wax distributions (Hollister et al., 2022; Thomas et al., 2016; Thomas et al., 2020).

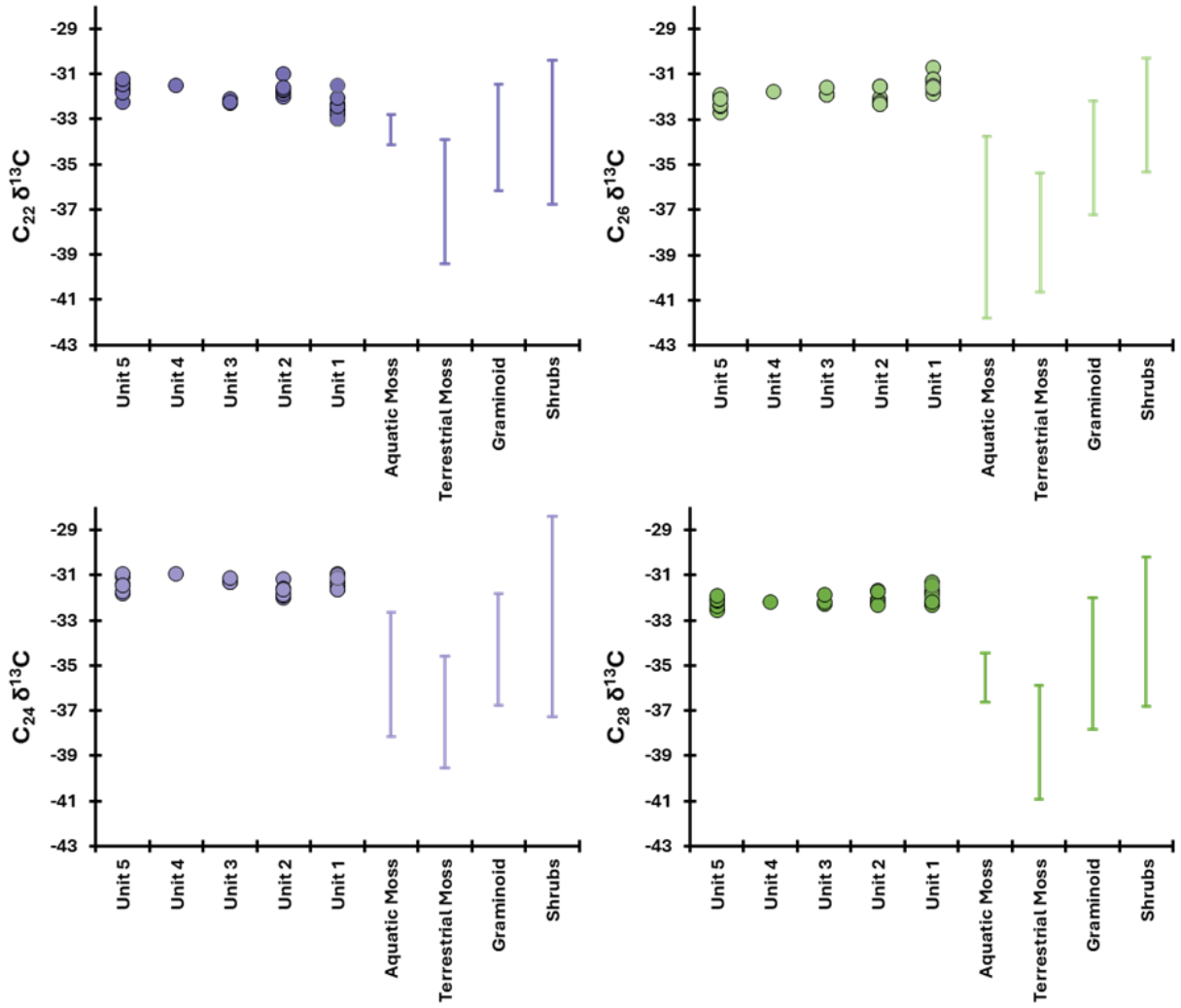

Figure S8. Plant wax $\delta^{13}C$ in Camp Century compared with modern $\delta^{13}C$ distributions in Arctic plants (Hollister et al., 2022).

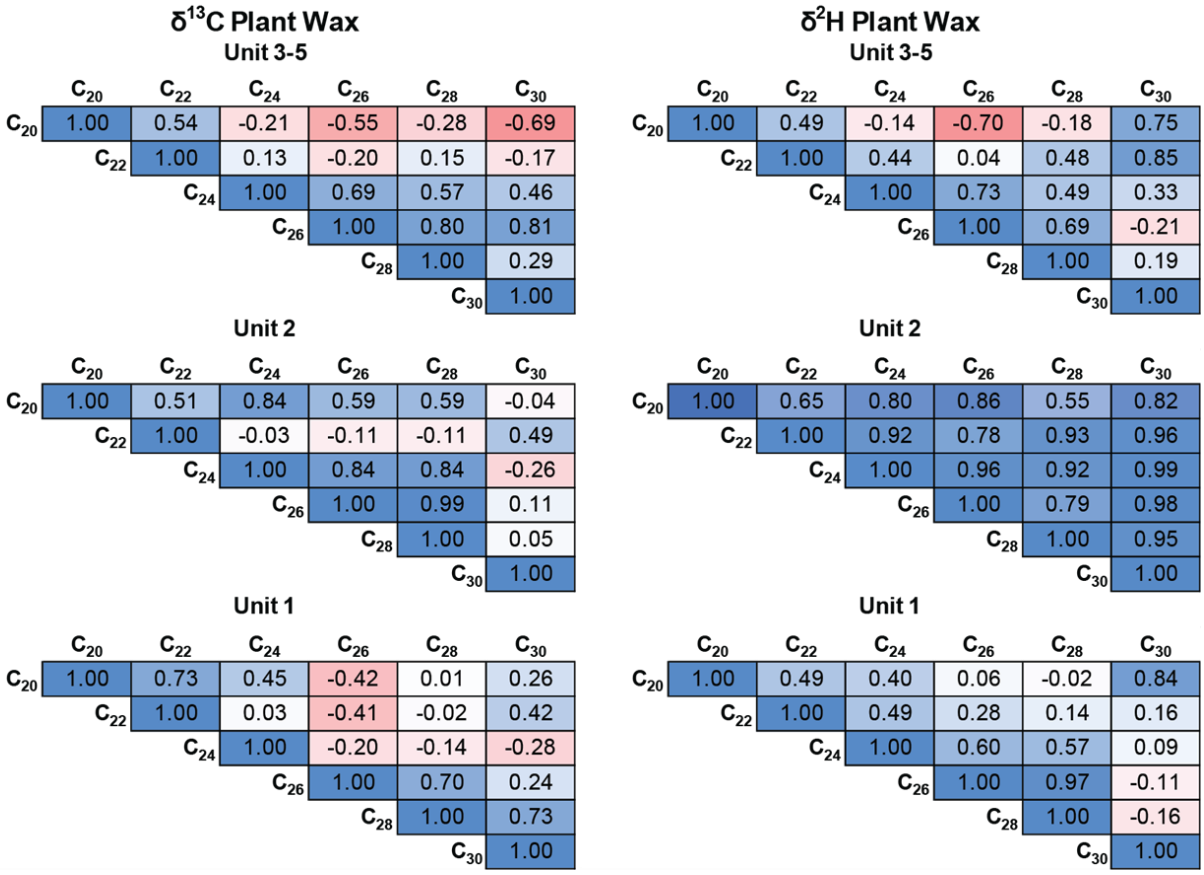

Figure S9. Correlation matrix of $\delta^{13}C$ and $\delta^{2}H$ across *n*-alkanoic acid chain lengths in different stratigraphic units.

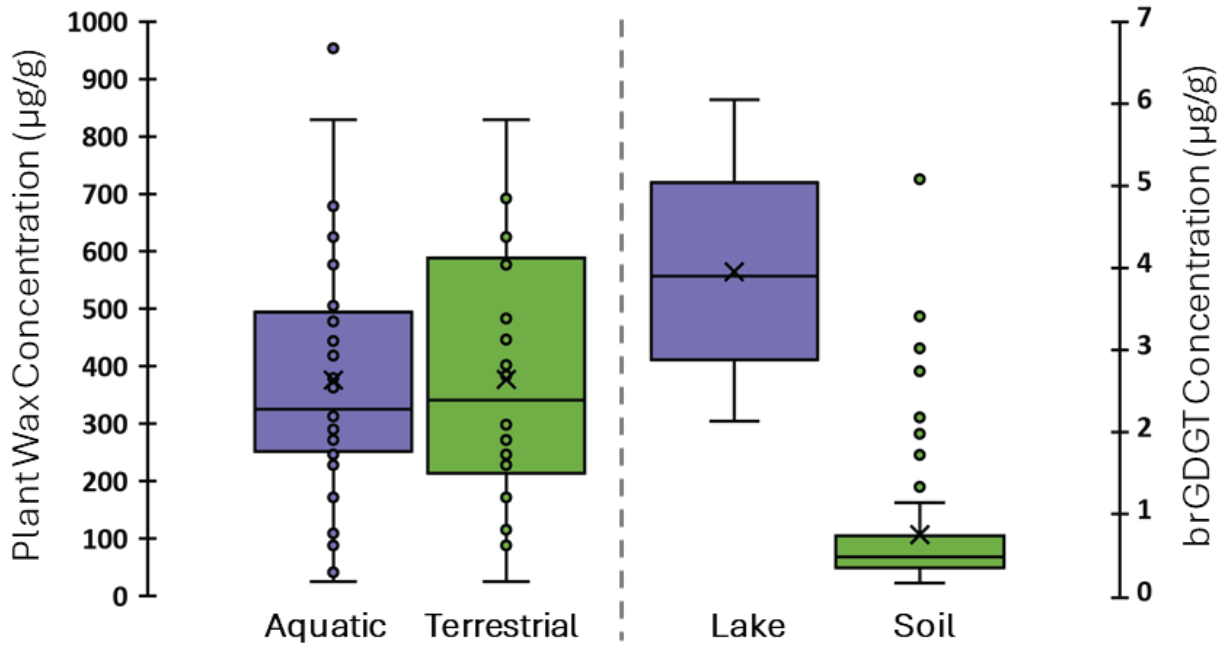

Figure S10. Distribution of plant wax and brGDGT concentrations in aquatic/lake and terrestrial/soil settings (Guo et al., 2020; Hollister et al., 2022; Martínez-Sosa et al., 2021). Box plots illustrate mean (x'es), median and interquartile range (line and box), 5th and 95th percentile (whiskers), and outliers (dots).

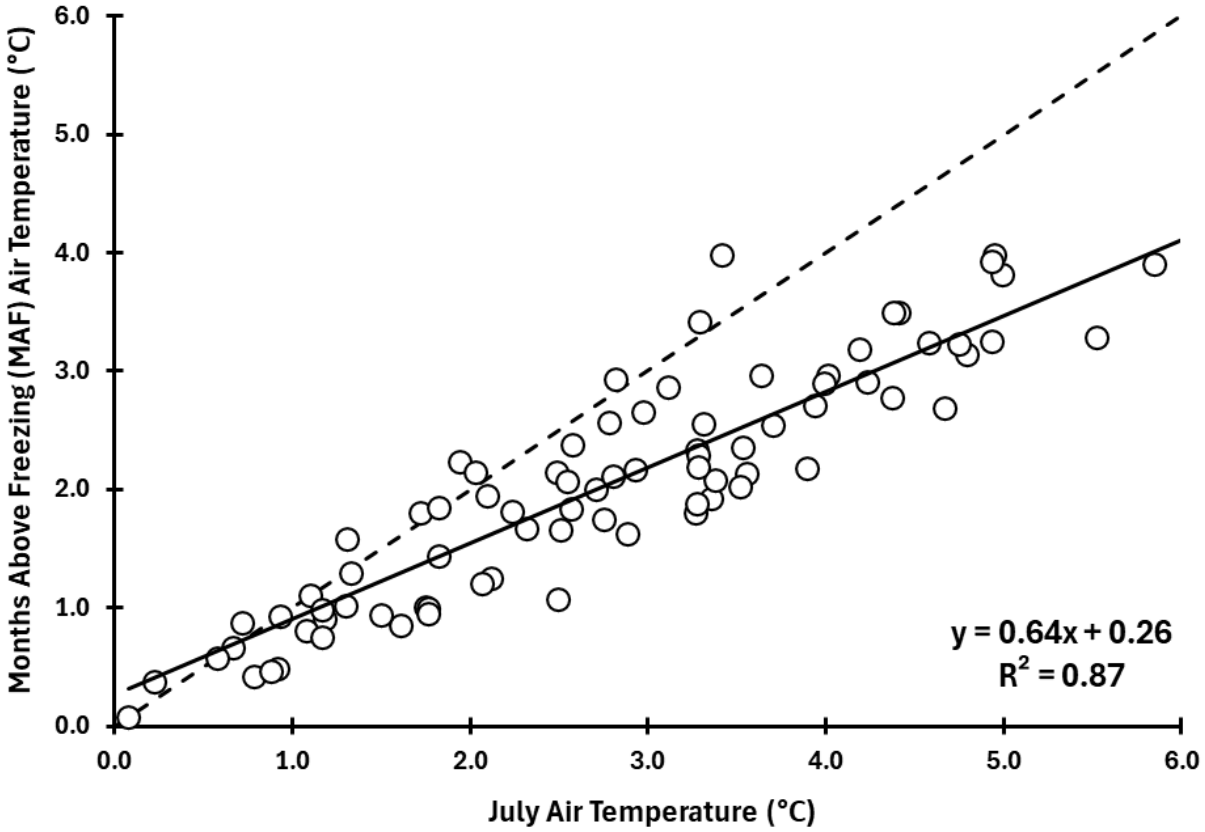

Figure S11. Linear relationship between July air temperature and months above freezing (MAF) at Pituffik Base Station based on ERA5 reanalysis data (Hersbach et al., 2020).

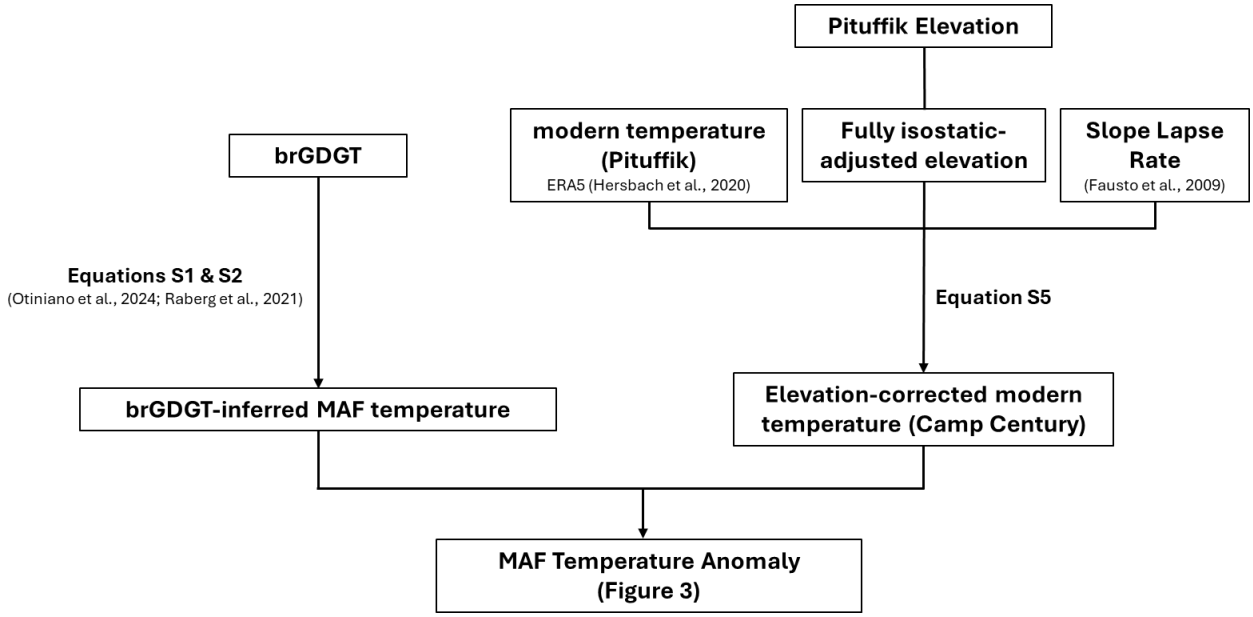

Figure S12. Schematic overview of the analytical framework used to reconstruct temperature and anomalies at Camp Century

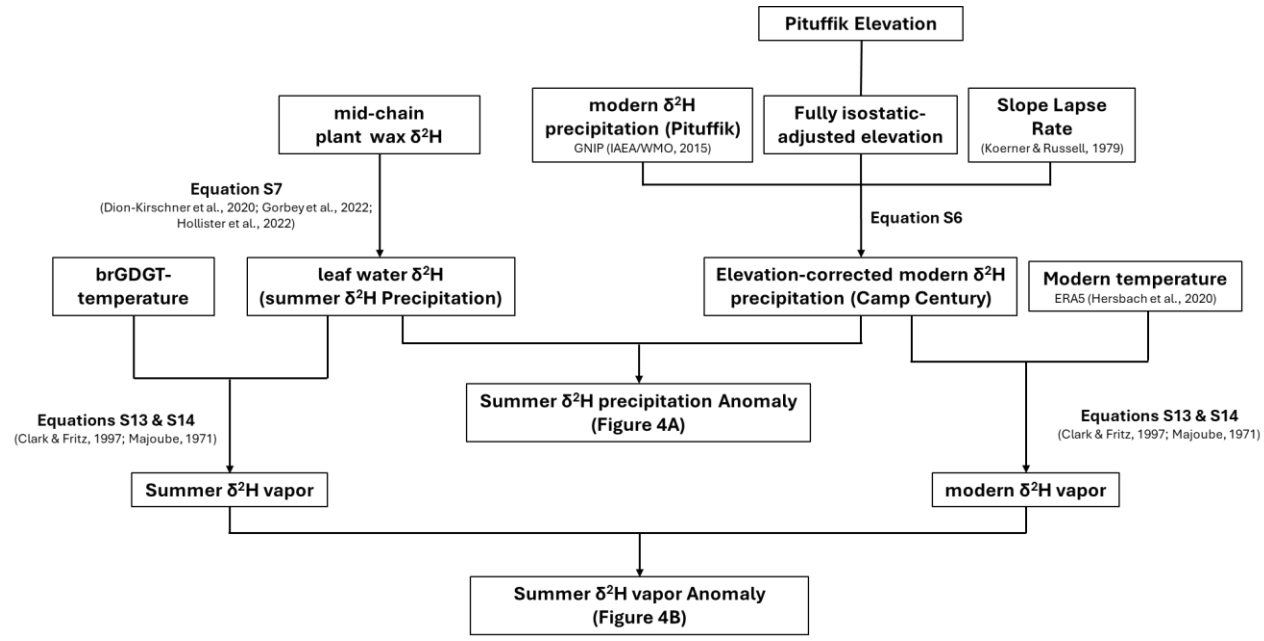

Figure S13. Schematic overview of the analytical framework used to reconstruct summer δ^2H precipitation and summer δ^2H vapor values and anomalies at Camp Century

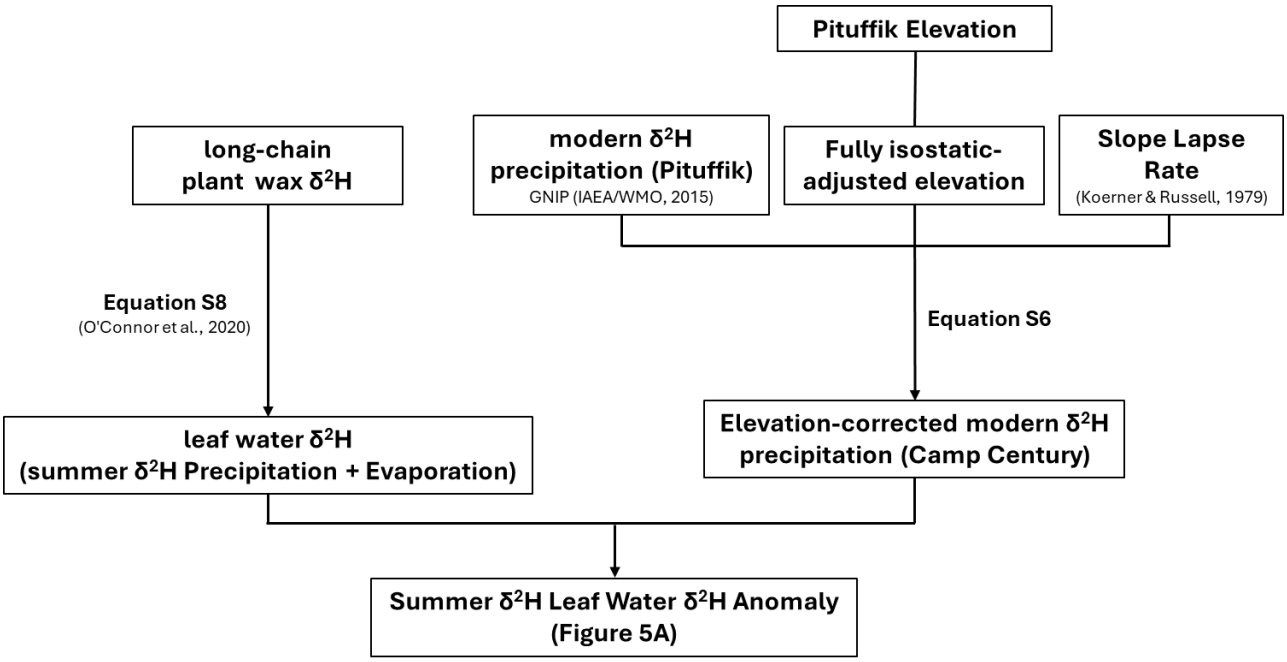

Figure S14. Schematic overview of the analytical framework used to reconstruct leaf water δ^2H anomalies at Camp Century

Table S1. Site locations and data sources for modern temperature values at each site.

Site Name	Latitude (°N)	Longitude (°E)	Elevation (m)	Time Period	Source	Notes
Pituffik Space Base	76.531	-68.703	77	1950-2000	ERA5 Climate Reanalyzer (Hersbach et al., 2020)	-
GISP2_Kobashi et al.	72.580	-38.480	3245	1988-2015 "the recent decades"	(Kobashi et al., 2017)	-
GISP2_Buizert et al.	72.580	-38.480	3245	1960-2000	(Buizert et al., 2018)	-
NGRIP_Buizert et al.	75.1	-42.32	2954	1960-2000	(Buizert et al., 2018)	-
NEEM_Buizert et al.	77.45	-51.06	2475	1960-2000	(Buizert et al., 2018)	-
Lake 578	61.080	-45.620	155	1950-2000	ERA5 Climate Reanalyzer (Hersbach et al., 2020)	-
Bullet Lake	63.982	-49.537	944	1950-2000	ERA5 Climate Reanalyzer (Hersbach et al., 2020)	Nearest Grid Cell*
Marshall Lake	64.464	-49.431	862	1950-2000	ERA5 Climate Reanalyzer (Hersbach et al., 2020)	Nearest Grid Cell*
Rosaea Lake	66.982	-53.718	228	1950-2000	ERA5 Climate Reanalyzer (Hersbach et al., 2020)	-
Lake Gus	67.032	-52.427	300	1950-2000	ERA5 Climate Reanalyzer (Hersbach et al., 2020)	-
Lake N3	68.636	-50.980	59	1950-2000	ERA5 Climate Reanalyzer (Hersbach et al., 2020)	-
Pluto Lake	69.110	-51.035	190	1950-2000	ERA5 Climate Reanalyzer (Hersbach et al., 2020)	-
Sikuiui Lake	70.218	-51.122	604	1950-2000	ERA5 Climate Reanalyzer (Hersbach et al., 2020)	-
North Lake	69.228	-50.927	285	1950-2000	ERA5 Climate Reanalyzer (Hersbach et al., 2020)	-
Last Chance Lake	70.906	-25.569	660	1950-2000	ERA5 Climate Reanalyzer (Hersbach et al., 2020)	-
Delta Sø	76.759	-67.610	250	1950-2000	ERA5 Climate Reanalyzer (Hersbach et al., 2020)	Pituffik Station**
Wax Lips Lake	76.852	-66.959	517	1950-2000	ERA5 Climate Reanalyzer (Hersbach et al., 2020)	Pituffik Station**
Jameson Land	71.167	-23.500	196	1950-2000	ERA5 Climate Reanalyzer (Hersbach et al., 2020)	-
Thule	76.450	-69.583	77	1950-2000	ERA5 Climate Reanalyzer (Hersbach et al., 2020)	-
Pingorsuit	76.410	-68.660	530	1950-2000	ERA5 Climate Reanalyzer (Hersbach et al., 2020)	-
Store Koldeway	76.750	-19.167		1950-2000	ERA5 Climate Reanalyzer (Hersbach et al., 2020)	-
Kap København	82.869	22.669		1950-2000	ERA5 Climate Reanalyzer (Hersbach et al., 2020)	-
íle de France	63.982	-49.537	944	1950-2000	ERA5 Climate Reanalyzer (Hersbach et al., 2020)	-

*Nearest grid cell not covered by ice

** Mean summer temperatures at these sites are similar to or warmer than Pituffik Station (Axford et al., 2019; McFarlin et al., 2018). Coastal observations are used as representative values since ERA5 does not resolve this location due to large grid cells.

Table S2. Site locations and data sources for modern isotope values at each site.

Site Name	Latitude (°N)	Longitude (°E)	Elevation (m)	Time Period	Source
Pituffik Space Base	76.531	-68.703	77	1966-1969	GNIP (IAEA/WMO, 2015)
Dye-3	65.183	-43.817	2490	1950-1970	(Dansgaard et al., 1982; Vinther et al., 2009)
Renland	71.270	-26.730	2350	1950-1970	(Vinther et al., 2009)
GISP2	72.580	-38.480	3245	1950-1987	(Grootes & Stuiver, 1999)
GRIP	72.583	-37.633	3230	1950-1970	(Johnsen et al., 1997)
NGRIP	75.100	-42.320	2954	1950-1990	(Andersen et al., 2004)
Camp Century	77.317	-61.133	1890	(20thCentury up till then)	(Dansgaard et al., 1969)
NEEM	77.450	-51.060	2475	1960-2017	(Dahl-Jensen et al., 2013; Schüpbach et al., 2018)
Flower Valley Lake	65.610	-37.694	73	1960-2017	GNIP, OIPC ((Bowen, 2017; Bowen et al., 2005; IAEA/WMO, 2015)
Lake N3	68.636	-50.980	59	1960-2017	GNIP, OIPC ((Bowen, 2017; Bowen et al., 2005; IAEA/WMO, 2015)
Pluto Lake	69.110	-51.035	190	1960-2017	GNIP, OIPC ((Bowen, 2017; Bowen et al., 2005; IAEA/WMO, 2015)
Secret Lake	76.580	-68.659	250	1960-2017	GNIP, OIPC ((Bowen, 2017; Bowen et al., 2005; IAEA/WMO, 2015)
Trifna So	79.990	-22.850	561	1960-2017	GNIP, OIPC ((Bowen, 2017; Bowen et al., 2005; IAEA/WMO, 2015)
Site 646 (ODP)	60.058 to 62.705	-45.107 to -41.919	-	1960-2017	GNIP, OIPC ((Bowen, 2017; Bowen et al., 2005; IAEA/WMO, 2015)

Table S3. Biosynthetic hydrogen isotope fractionation factor (ε_{bio}) between long-chain plant wax and leaf water in high-latitude sites (>50°N), compiled from several locations (Berke et al., 2019; Gao et al., 2014; Nichols et al., 2010; O'Connor et al., 2020)

Plant Forms	$Epsilon_{C28LeafWater}$	$Epsilon_{C28LeafWater\_err}$	$Epsilon_{C29LeafWater}$	$Epsilon_{C29LeafWater\_err}$
Graminoids	-175	4	-170	8
Shrubs	-155	5	-135	4
Forbs	-150	6	-144	4
Vascular Plants	-160	9	-150	12
Mosses	-170			

Table S4. Estimated ε_{bio} values at high-latitude (>50°N) for cold- and warm-regions based on vegetation, where cold regions are dominated by mosses with minimal vascular plants and warm regions have higher percentages of vascular plants (Bennike, 2000; Berke et al., 2019; Gao et al., 2014; Kusch et al., 2019; Nichols et al., 2010; O'Connor et al., 2020).

	$Epsilon_{C28LeafWater}$	$Epsilon_{C28LeafWater\_err}$	$Epsilon_{C29LeafWater}$	$Epsilon_{C29LeafWater\_err}$
Cold Region	98% Moss; 2% Vascular Plants		98% Moss; 1% Shrubs;1% Forbs	
	-170	6	-169	6
Warmer Region	25% Moss; 75% Vascular Plants		25% Moss; 75% Vascular Plants	
	-168	9	-165	12

References

Acharya, S., Cluett, A. A., Grogan, A. L., Briner, J. P., Castañeda, I. S., & Thomas, E. K. (2025). Holocene temperatures in southwestern Greenland controlled by topography, ice sheet proximity and oceanic conditions. *EGUsphere, 2025*, 1-32. https://egusphere.copernicus.org/preprints/2025/egusphere-2025-3113/

Andersen, K. K., Azuma, N., Barnola, J. M., Bigler, M., Biscaye, P., Caillon, N., et al. (2004). High-resolution record of Northern Hemisphere climate extending into the last interglacial period. *Nature, 431*(7005), 147-151. https://doi.org/10.1038/nature02805

Atti, S., Bennike, O., & Weckström, K. (2024). Cladocerans and diatoms from an Early Pleistocene interglacial deposit at Pingorsuit, North-West Greenland. *Journal of Paleolimnology, 72*(3), 331-341. https://doi.org/10.1007/s10933-024-00333-z

Axford, Y., de Vernal, A., & Osterberg, E. C. (2021). Past Warmth and Its Impacts During the Holocene Thermal Maximum in Greenland. *Annual Review of Earth and Planetary Sciences, 49*(Volume 49, 2021), 279-307. https://www.annualreviews.org/content/journals/10.1146/annurev-earth-081420-063858

Axford, Y., Lasher, G. E., Kelly, M. A., Osterberg, E. C., Landis, J., Schellinger, G. C., et al. (2019). Holocene temperature history of northwest Greenland – With new ice cap constraints and chironomid assemblages from Deltasø. *Quaternary Science Reviews, 215*, 160-172. https://www.sciencedirect.com/science/article/pii/S0277379119302021

Axford, Y., Levy, L. B., Kelly, M. A., Francis, D. R., Hall, B. L., Langdon, P. G., & Lowell, T. V. (2017). Timing and magnitude of early to middle Holocene warming in East Greenland inferred from chironomids. *Boreas, 46*(4), 678-687. https://onlinelibrary.wiley.com/doi/abs/10.1111/bor.12247

Axford, Y., Losee, S., Briner, J. P., Francis, D. R., Langdon, P. G., & Walker, I. R. (2013). Holocene temperature history at the western Greenland Ice Sheet margin reconstructed from lake sediments. *Quaternary Science Reviews, 59*, 87-100. https://www.sciencedirect.com/science/article/pii/S0277379112004209

Balascio, N. L., D'Andrea, W. J., Bradley, R. S., & Perren, B. B. (2013). Biogeochemical evidence for hydrologic changes during the Holocene in a lake sediment record from southeast Greenland. *The Holocene, 23*(10), 1428-1439. https://doi.org/10.1177/0959683613493938

Bennike, O. (1990). The Kap København Formation: stratigraphy and palaeobotany of a Plio-Pleistocene sequence in Peary Land, North Greenland. *Meddelelser om Grønland. Geoscience, 23*, 85 pp. https://tidsskrift.dk/meddrgroenland_geosci/article/view/141978

Bennike, O. (2000). Palaeoecological studies of Holocene lake sediments from west Greenland. *Palaeogeography, Palaeoclimatology, Palaeoecology, 155*(3), 285-304. https://www.sciencedirect.com/science/article/pii/S0031018299001212

Bennike, O., Abrahamsen, N., Bak, M., Israelson, C., Konradi, P., Matthiessen, J., & Witkowski, A. (2002). A multi-proxy study of Pliocene sediments from Île de France, North-East Greenland. *Palaeogeography, Palaeoclimatology, Palaeoecology, 186*(1), 1-23. https://www.sciencedirect.com/science/article/pii/S003101820200439X

Bennike, O., & Böcher, J. (1992). Early Weichselian interstadial land biotas at Thule, Northwest Greenland. *Boreas, 21*(2), 111-118. https://onlinelibrary.wiley.com/doi/abs/10.1111/j.1502-3885.1992.tb00019.x

Bennike, O., & Böcher, J. (1994). Land biotas of the last interglacial/glacial cycle on Jameson Land, East Greenland. *Boreas, 23*(4), 479-487. https://onlinelibrary.wiley.com/doi/abs/10.1111/j.1502-3885.1994.tb00615.x

Bennike, O., Colgan, W., Hedenäs, L., Heiri, O., Lemdahl, G., Wiberg-Larsen, P., et al. (2023). An Early Pleistocene interglacial deposit at Pingorsuit, North-West Greenland. *Boreas, 52*(1), 27-41. https://onlinelibrary.wiley.com/doi/abs/10.1111/bor.12596

Bennike, O., Knudsen, K. L., Abrahamsen, N., Böcher, J., Cremer, H., & Wagner, B. (2010). Early Pleistocene sediments on Store Koldewey, northeast Greenland. *Boreas, 39*(3), 603-619. https://onlinelibrary.wiley.com/doi/abs/10.1111/j.1502-3885.2010.00147.x

Berke, M. A., Cartagena Sierra, A., Bush, R., Cheah, D., & O'Connor, K. (2019). Controls on leaf wax fractionation and δ2H values in tundra vascular plants from western Greenland. *Geochimica et Cosmochimica Acta, 244*, 565-583. https://www.sciencedirect.com/science/article/pii/S0016703718306069

Bierman, P. R., Christ, A. J., Collins, C. M., Mastro, H. M., Souza, J., Blard, P. H., et al. (2024). Scientific history, sampling approach, and physical characterization of the Camp Century sub-glacial sediment core, a rare archive from beneath the Greenland Ice Sheet. *EGUsphere, 2024*, 1-28. https://egusphere.copernicus.org/preprints/2024/egusphere-2023-2922/

Blaga, C. I., Reichart, G.-J., Heiri, O., & Sinninghe Damsté, J. S. (2009). Tetraether membrane lipid distributions in water-column particulate matter and sediments: a study of 47 European lakes along a north–south transect. *Journal of Paleolimnology, 41*(3), 523-540. https://doi.org/10.1007/s10933-008-9242-2

Bowen, G. (2017). The Online Isotopes in Precipitation Calculator. Retrieved from http://www.waterisotopes.org

Bowen, G. J., Wassenaar, L. I., & Hobson, K. A. (2005). Global application of stable hydrogen and oxygen isotopes to wildlife forensics. *Oecologia, 143*(3), 337-348. https://doi.org/10.1007/s00442-004-1813-y

Briner, J. P., McKay, N. P., Axford, Y., Bennike, O., Bradley, R. S., de Vernal, A., et al. (2016). Holocene climate change in Arctic Canada and Greenland. *Quaternary Science Reviews, 147*, 340-364. https://www.sciencedirect.com/science/article/pii/S0277379116300427

Brodersen, K. P., & Bennike, O. (2003). Interglacial Chironomidae (Diptera) from Thule, Northwest Greenland: matching modern analogues to fossil assemblages. *Boreas, 32*(4), 560-565. https://onlinelibrary.wiley.com/doi/abs/10.1111/j.1502-3885.2003.tb01235.x

Buizert, C., Keisling, B. A., Box, J. E., He, F., Carlson, A. E., Sinclair, G., & DeConto, R. M. (2018). Greenland-Wide Seasonal Temperatures During the Last Deglaciation. *Geophysical Research Letters, 45*(4), 1905-1914. https://agupubs.onlinelibrary.wiley.com/doi/abs/10.1002/2017GL075601

CAVM Team (Cartographer). (2024). Raster Circumpolar Arctic Vegetation Map

Christ, A. J., Bierman, P. R., Schaefer, J. M., Dahl-Jensen, D., Steffensen, J. P., Corbett, L. B., et al. (2021). A multimillion-year-old record of Greenland vegetation and glacial history preserved in sediment beneath 1.4 km of ice at Camp Century. *Proceedings of the National Academy of Sciences, 118*(13), e2021442118. https://doi.org/10.1073/pnas.2021442118

Christ, A. J., Rittenour, T. M., Bierman, P. R., Keisling, B. A., Knutz, P. C., Thomsen, T. B., et al. (2023). Deglaciation of northwestern Greenland during Marine Isotope Stage 11. *Science, 381*(6655), 330-335. https://www.science.org/doi/abs/10.1126/science.ade4248

Clark, I. D., & Fritz, P. (1997). *Environmental Isotopes in Hydrogeology* (1st ed.). Boca Raton, FL: CRC Press.

Cluett, A. A., & Thomas, E. K. (2021). Summer warmth of the past six interglacials on Greenland. *Proceedings of the National Academy of Sciences, 118*(20), e2022916118. https://www.pnas.org/doi/abs/10.1073/pnas.2022916118

Cluett, A. A., Thomas, E. K., McKay, N. P., Cowling, O. C., Castañeda, I. S., & Morrill, C. (2023). Lake Dynamics Modulate the Air Temperature Variability Recorded by Sedimentary Aquatic Biomarkers: A Holocene Case Study From Western Greenland. *Journal of Geophysical Research: Biogeosciences, 128*(7), e2022JG007106. https://agupubs.onlinelibrary.wiley.com/doi/abs/10.1029/2022JG007106

Cluett, A. A., Thomas, E. K., Evans, S. M., & Keys, P. W. . (2021). Seasonal Variations in Moisture Origin Explain Spatial Contrast in Precipitation Isotope Seasonality on Coastal Western Greenland. *Journal of Geophysical Research: Biogeosciences, 126*(11).

Collins, C. M., Perdrial, N., Blard, P. H., Keulen, N., Mahaney, W. C., Mastro, H., et al. (2024). Characterization of the 1966 Camp Century Sub-Glacial Core: A Multiscale Analysis. *EGUsphere, 2024*, 1-33. https://egusphere.copernicus.org/preprints/2024/egusphere-2024-2194/

Cowling, O. C., Thomas, E. K., Svendsen, J. I., Mangerud, J., Haflidason, H., Regnéll, C., & Brendryen, J. (2022). Western Siberia experienced rapid shifts in moisture source and summer water balance during the last deglaciation and early Holocene. *Journal of Quaternary Science, 37*(5), 790-804. https://onlinelibrary.wiley.com/doi/abs/10.1002/jqs.3386

Dahl-Jensen, D., Albert, M. R., Aldahan, A., Azuma, N., Balslev-Clausen, D., Baumgartner, M., et al. (2013). Eemian interglacial reconstructed from a Greenland folded ice core. *Nature, 493*(7433), 489-494. https://doi.org/10.1038/nature11789

Dansgaard, W. (1964). Stable isotopes in precipitation. *Tellus, 16*(4), 436-468. https://onlinelibrary.wiley.com/doi/abs/10.1111/j.2153-3490.1964.tb00181.x

Dansgaard, W., Clausen, H. B., Gundestrup, N., Hammer, C. U., Johnsen, S. F., Kristinsdottir, P. M., & Reeh, N. (1982). A New Greenland Deep Ice Core. *Science, 218*(4579), 1273-1277. https://www.science.org/doi/abs/10.1126/science.218.4579.1273

Dansgaard, W., Johnsen, S. J., Møller, J., & Langway, C. C. (1969). One Thousand Centuries of Climatic Record from Camp Century on the Greenland Ice Sheet. *Science, 166*(3903), 377-381. https://www.science.org/doi/abs/10.1126/science.166.3903.377

De Jonge, C., Hopmans, E. C., Zell, C. I., Kim, J.-H., Schouten, S., & Sinninghe Damsté, J. S. (2014). Occurrence and abundance of 6-methyl branched glycerol dialkyl glycerol tetraethers in soils: Implications for palaeoclimate reconstruction. *Geochimica et Cosmochimica Acta, 141*, 97-112. https://www.sciencedirect.com/science/article/pii/S0016703714004141

Dion-Kirschner, H., McFarlin, J. M., Masterson, A. L., Axford, Y., & Osburn, M. R. (2020). Modern constraints on the sources and climate signals recorded by sedimentary plant waxes in west Greenland. *Geochimica et Cosmochimica Acta, 286*, 336-354. https://www.sciencedirect.com/science/article/pii/S0016703720304579

Ellehoj, M. D., Steen-Larsen, H. C., Johnsen, S. J., & Madsen, M. B. (2013). Ice-vapor equilibrium fractionation factor of hydrogen and oxygen isotopes: Experimental investigations and implications for stable water isotope studies. *Rapid Communications in Mass Spectrometry, 27*(19), 2149-2158. https://analyticalsciencejournals.onlinelibrary.wiley.com/doi/abs/10.1002/rcm.6668

Fausto, R. S., Ahlstrøm, A. P., Van As, D., Bøggild, C. E., & Johnsen, S. J. (2009). A new present-day temperature parameterization for Greenland. *Journal of Glaciology, 55*(189), 95-105. https://www.cambridge.org/core/product/A4C890F114971EF99BF0EF46140C8382

Gao, L., Edwards, E. J., Zeng, Y., & Huang, Y. (2014). Major Evolutionary Trends in Hydrogen Isotope Fractionation of Vascular Plant Leaf Waxes. *PLoS ONE, 9*(11), e122610.

Gao, L., Hou, J., Toney, J., MacDonald, D., & Huang, Y. (2011). Mathematical modeling of the aquatic macrophyte inputs of mid-chain n-alkyl lipids to lake sediments: Implications for interpreting compound specific hydrogen isotopic records. *Geochimica et Cosmochimica Acta, 75*(13), 3781-3791. https://www.sciencedirect.com/science/article/pii/S0016703711002274

Gimeno, L., Eiras-Barca, J., Durán-Quesada, A. M., Dominguez, F., van der Ent, R., Sodemann, H., et al. (2021). The residence time of water vapour in the atmosphere. *Nature Reviews Earth & Environment, 2*(8), 558-569. https://doi.org/10.1038/s43017-021-00181-9

Gorbey, D. B., Thomas, E. K., Sauer, P. E., Raynolds, M. K., Miller, G. H., Corcoran, M. C., et al. (2022). Modern Eastern Canadian Arctic Lake Water Isotopes Exhibit Latitudinal Patterns in Inflow Seasonality and Minimal Evaporative Enrichment. *Paleoceanography and Paleoclimatology, 37*(5), e2021PA004384. https://agupubs.onlinelibrary.wiley.com/doi/abs/10.1029/2021PA004384

Grootes, P. M., & Stuiver, M. (1997). Oxygen 18/16 variability in Greenland snow and ice with 10−3- to 105-year time resolution. *Journal of Geophysical Research: Oceans, 102*(C12), 26455-26470. https://agupubs.onlinelibrary.wiley.com/doi/abs/10.1029/97JC00880

Grootes, P. M., & Stuiver, M. (1999). *GISP2 Oxygen Isotope Data (1 year averages)*. Retrieved from: https://doi.org/10.1594/PANGAEA.55532

Guo, J., Glendell, M., Meersmans, J., Kirkels, F., Middelburg, J. J., & Peterse, F. (2020). Assessing branched tetraether lipids as tracers of soil organic carbon transport through the Carminowe Creek catchment (southwest England). *Biogeosciences, 17*(12), 3183-3201. https://bg.copernicus.org/articles/17/3183/2020/

Hedenäs, L. (1994). Bryophytes from the last interglacial/glacial cycle, Jameson Land, East Greenland. *Boreas, 23*(4), 488-494. https://onlinelibrary.wiley.com/doi/abs/10.1111/j.1502-3885.1994.tb00616.x

Hedenäs, L., & Bennike, O. (2003). Moss Remains from the Last Interglacial at Thule, NW Greenland. *Lindbergia, 28*(2), 52-58. http://www.jstor.org/stable/20150125

Hersbach, H., Bell, B., Berrisford, P., Hirahara, S., Horányi, A., Muñoz-Sabater, J., et al. (2020). The ERA5 global reanalysis. *Quarterly Journal of the Royal Meteorological Society, 146*(730), 1999-2049. https://rmets.onlinelibrary.wiley.com/doi/abs/10.1002/qj.3803

Hollister, K. V., Thomas, E. K., Raynolds, M. K., Bültmann, H., Raberg, J. H., Miller, G. H., & Sepúlveda, J. (2022). Aquatic and Terrestrial Plant Contributions to Sedimentary Plant Waxes in a Modern Arctic Lake Setting. *Journal of Geophysical Research: Biogeosciences, 127*(8), e2022JG006903. https://agupubs.onlinelibrary.wiley.com/doi/abs/10.1029/2022JG006903

Hopmans, E. C., Schouten, S., & Sinninghe Damsté, J. S. (2016). The effect of improved chromatography on GDGT-based palaeoproxies. *Organic Geochemistry, 93*, 1-6. https://www.sciencedirect.com/science/article/pii/S0146638015002387

Huguet, C., Hopmans, E. C., Febo-Ayala, W., Thompson, D. H., Sinninghe Damsté, J. S., & Schouten, S. (2006). An improved method to determine the absolute abundance of glycerol dibiphytanyl glycerol tetraether lipids. *Organic Geochemistry, 37*(9), 1036-1041. https://www.sciencedirect.com/science/article/pii/S0146638006001094

IAEA/WMO. (2015). *Global Network of Isotopes in Precipitation (GNIP) Database* [data set]. Retrieved from: http://www.iaea.org/water

Johnsen, S. J., Clausen, H. B., Dansgaard, W., Gundestrup, N. S., Hammer, C. U., Andersen, U., et al. (1997). The δ18O record along the Greenland Ice Core Project deep ice core and the problem of possible Eemian climatic instability. *Journal of Geophysical Research: Oceans, 102*(C12), 26397-26410. https://agupubs.onlinelibrary.wiley.com/doi/abs/10.1029/97JC00167

Kobashi, T., Menviel, L., Jeltsch-Thömmes, A., Vinther, B. M., Box, J. E., Muscheler, R., et al. (2017). Volcanic influence on centennial to millennial Holocene Greenland temperature change. *Scientific Reports, 7*(1), 1441. https://doi.org/10.1038/s41598-017-01451-7

Koerner, R., & Russell, R. D. (1979). δ18O variations in snow on the Devon Island ice cap, Northwest Territories, Canada. *Canadian Journal of Earth Sciences, 16*(7), 1419-1427. https://cdnsciencepub.com/doi/abs/10.1139/e79-126

Kusch, S., Bennike, O., Wagner, B., Lenz, M., Steffen, I., & Rethemeyer, J. (2019). Holocene environmental history in high-Arctic North Greenland revealed by a combined biomarker and macrofossil approach. *Boreas, 48*(2), 273-286. https://onlinelibrary.wiley.com/doi/abs/10.1111/bor.12377

Lasher, G. E., Axford, Y., McFarlin, J. M., Kelly, M. A., Osterberg, E. C., & Berkelhammer, M. B. (2017). Holocene temperatures and isotopes of precipitation in Northwest Greenland recorded in lacustrine organic materials. *Quaternary Science Reviews, 170*, 45-55. https://www.sciencedirect.com/science/article/pii/S0277379116305650

Lee, H., Feakins, S. J., Lu, Z., Schimmelmann, A., Sessions, A. L., Tierney, J. E., & Williams, T. J. (2017). Comparison of three methods for the methylation of aliphatic and aromatic compounds. *Rapid Commun Mass Spectrom, 31*(19), 1633-1640.

Lindberg, K. R., Daniels, W. C., Castañeda, I. S., & Brigham-Grette, J. (2022). Biomarker proxy records of Arctic climate change during the Mid-Pleistocene transition from Lake El'gygytgyn (Far East Russia). *Clim. Past, 18*(3), 559-577. https://cp.copernicus.org/articles/18/559/2022/

Majoube, M. (1971). Fractionnement en oxygène 18 et en deutérium entre l'eau et sa vapeur. *J. Chim. Phys., 68*, 1423-1436. https://doi.org/10.1051/jcp/1971681423

Martin, K. C., Buizert, C., Brook, E., Williams, O. L., Edwards, J. S., Riddell-Young, B., et al. (2024). Greenland Ice Cores Reveal a South-To-North Difference in Holocene Thermal Maximum Timings. *Geophysical Research Letters, 51*(24), e2024GL111405. https://agupubs.onlinelibrary.wiley.com/doi/abs/10.1029/2024GL111405

Martínez-Sosa, P., Tierney, J. E., Stefanescu, I. C., Dearing Crampton-Flood, E., Shuman, B. N., & Routson, C. (2021). A global Bayesian temperature calibration for lacustrine brGDGTs. *Geochimica et Cosmochimica Acta, 305*, 87-105. https://www.sciencedirect.com/science/article/pii/S0016703721002635

McFarlin, J. M., Axford, Y., Kusch, S., Masterson, A. L., Lasher, G. E., & Osburn, M. R. (2023). Aquatic plant wax hydrogen and carbon isotopes in Greenland lakes record shifts in methane cycling during past Holocene warming. *Science Advances, 9*(39), eadh9704. https://www.science.org/doi/abs/10.1126/sciadv.adh9704

McFarlin, J. M., Axford, Y., Osburn, M. R., Kelly, M. A., Osterberg, E. C., & Farnsworth, L. B. (2018). Pronounced summer warming in northwest Greenland during the Holocene and Last Interglacial. *Proceedings of the National Academy of Sciences, 115*(25), 6357-6362. https://www.pnas.org/doi/abs/10.1073/pnas.1720420115

Morlighem, M., Williams, C. N., Rignot, E., An, L., Arndt, J. E., Bamber, J. L., et al. (2017). BedMachine v3: Complete Bed Topography and Ocean Bathymetry Mapping of Greenland From Multibeam Echo Sounding Combined With Mass Conservation. *Geophysical Research Letters, 44*(21), 11,051-011,061. https://agupubs.onlinelibrary.wiley.com/doi/abs/10.1002/2017GL074954

Naafs, B. D. A., Inglis, G. N., Zheng, Y., Amesbury, M. J., Biester, H., Bindler, R., et al. (2017). Introducing global peat-specific temperature and pH calibrations based on brGDGT bacterial lipids. *Geochimica et Cosmochimica Acta, 208*, 285-301. https://www.sciencedirect.com/science/article/pii/S0016703717300522

Nichols, J., Booth, R. K., Jackson, S. T., Pendall, E. G., & Huang, Y. (2010). Differential hydrogen isotopic ratios of Sphagnum and vascular plant biomarkers in ombrotrophic peatlands as a quantitative proxy for precipitation—evaporation balance. *Geochimica et Cosmochimica Acta, 74*(4), 1407-1416. https://www.sciencedirect.com/science/article/pii/S001670370900711X

O'Connor, K. F., Berke, M. A., & Ziolkowski, L. A. (2020). Hydrogen isotope fractionation in modern plants along a boreal-tundra transect in Alaska. *Organic Geochemistry, 147*, 104064. https://www.sciencedirect.com/science/article/pii/S0146638020300991

Otiniano, G. A., Porter, T. J., Buceta, R. E., Bergman, M. E., & Phillips, M. A. (2023). Climatic and environmentally driven variability in lacustrine brGDGT distributions at local to regional scales in Alaska and northwestern Canada. *Organic Geochemistry, 181*, 104604. https://www.sciencedirect.com/science/article/pii/S0146638023000505

Otiniano, G. A., Porter, T. J., Phillips, M. A., Juutinen, S., Weckström, J. B., & Heikkilä, M. P. (2024). Reconstructing warm-season temperatures using brGDGTs and assessing biases in Holocene temperature records in northern Fennoscandia. *Quaternary Science Reviews, 329*, 108555. https://www.sciencedirect.com/science/article/pii/S0277379124000568

Paxman, G. J. G., Austermann, J., & Hollyday, A. (2022). Total isostatic response to the complete unloading of the Greenland and Antarctic Ice Sheets. *Scientific Reports, 12*(1), 11399. https://doi.org/10.1038/s41598-022-15440-y

Poage, M. A., & Chamberlain, C. P. (2001). Empirical Relationships Between Elevation and the Stable Isotope Composition of Precipitation and Surface Waters: Considerations for Studies of Paleoelevation Change. *American Journal of Science, 301*(1), 1-15.

Raberg, J. H., Harning, D. J., Crump, S. E., de Wet, G., Blumm, A., Kopf, S., et al. (2021). Revised fractional abundances and warm-season temperatures substantially improve brGDGT calibrations in lake sediments. *Biogeosciences, 18*(12), 3579-3603. https://bg.copernicus.org/articles/18/3579/2021/

Raynolds, M. K., Walker, D. A., Balser, A., Bay, C., Campbell, M., Cherosov, M. M., et al. (2019). A raster version of the Circumpolar Arctic Vegetation Map (CAVM). *Remote Sensing of Environment, 232*, 111297. https://www.sciencedirect.com/science/article/pii/S0034425719303165

Russell, J. M., Hopmans, E. C., Loomis, S. E., Liang, J., & Sinninghe Damsté, J. S. (2018). Distributions of 5- and 6-methyl branched glycerol dialkyl glycerol tetraethers (brGDGTs) in East African lake sediment: Effects of temperature, pH, and new lacustrine paleotemperature calibrations. *Organic Geochemistry, 117*, 56-69. https://www.sciencedirect.com/science/article/pii/S0146638017304394

Sachse, D., Isabelle, B., Bowen, G., Chikaraishi, Y., Dawson, T., Feakins, S., et al. (2012). Molecular Paleohydrology: Interpreting the Hydrogen-Isotopic Composition of Lipid Biomarkers from Photosynthesizing Organisms. *Annual Review of Earth and Planetary Sciences, 40*, 221-249.

Schneider, T., Castañeda, I. S., Zhao, B., Krüger, S., Salacup, J. M., & Bradley, R. S. (2024). Tracing Holocene temperatures and human impact in a Greenlandic Lake: Novel insights from hyperspectral imaging and lipid biomarkers. *Quaternary Science Reviews, 339*, 108851. https://www.sciencedirect.com/science/article/pii/S0277379124003524

Schouten, S., Hopmans, E. C., & Sinninghe Damsté, J. S. (2013). The organic geochemistry of glycerol dialkyl glycerol tetraether lipids: A review. *Organic Geochemistry, 54*, 19-61. https://www.sciencedirect.com/science/article/pii/S0146638012001982

Schüpbach, S., Fischer, H., Bigler, M., Erhardt, T., Gfeller, G., Leuenberger, D., et al. (2018). Greenland records of aerosol source and atmospheric lifetime changes from the Eemian to the Holocene. *Nature Communications, 9*(1), 1476. https://doi.org/10.1038/s41467-018-03924-3

Stuiver, M., & Grootes, P. M. (2000). GISP2 Oxygen Isotope Ratios. *Quaternary Research, 53*(3), 277-284. https://www.sciencedirect.com/science/article/pii/S0033589400921276

Thomas, E., Briner, J., Ryan-Henry, J., & Huang, Y. (2016). A major increase in winter snowfall during the middle Holocene on western Greenland caused by reduced sea ice in Baffin Bay and the Labrador Sea: Holocene Sea Ice Loss Caused More Snow. *Geophysical Research Letters, 43*.

Thomas, E. K., Castañeda, I. S., McKay, N. P., Briner, J. P., Salacup, J. M., Nguyen, K. Q., & Schweinsberg, A. D. (2018). A Wetter Arctic Coincident With Hemispheric Warming 8,000 Years Ago. *Geophysical Research Letters, 45*(19), 10,637-610,647. https://agupubs.onlinelibrary.wiley.com/doi/abs/10.1029/2018GL079517

Thomas, E. K., Hollister, K. V., Cluett, A. A., & Corcoran, M. C. (2020). Reconstructing Arctic Precipitation Seasonality Using Aquatic Leaf Wax δ2H in Lakes With Contrasting Residence Times. *Paleoceanography and Paleoclimatology, 35*.

Vinther, B. M., Buchardt, S. L., Clausen, H. B., Dahl-Jensen, D., Johnsen, S. J., Fisher, D. A., et al. (2009). Holocene thinning of the Greenland ice sheet. *Nature, 461*(7262), 385-388. https://doi.org/10.1038/nature08355

Zhao, B., Russell, J. M., Tsai, V. C., Blaus, A., Parish, M. C., Liang, J., et al. (2023). Evaluating global temperature calibrations for lacustrine branched GDGTs: Seasonal variability, paleoclimate implications, and future directions. *Quaternary Science Reviews, 310*, 108124. https://www.sciencedirect.com/science/article/pii/S0277379123001725